Degradation and Erosion of Metal–Organic Frameworks: Comparative Study of a NanoMIL-100 Drug Delivery System

Mai Dang Le Vuong, Yuliia Horbenko, Mathieu Frégnaux, Ioanna Christodoulou, Charlotte Martineau-Corcos, Pierre Levitz, Anne-Laure Rollet, Ruxandra Gref, Mohamed Haouas

Degradation and Erosion of Metal-Organic Framework: Comparative Study of NanoMIL-100 Drug Delivery System

Mai Dang Le Vuong,[a,b,c] Yuliia Horbenko,[a] Mathieu Frégnaux,[a] Ioanna Christodoulou,[b] Charlotte Martineau-Corcos,[a,d] Pierre Levitz,[c] Anne-Laure Rollet,[c] Ruxandra Gref*[b] and Mohamed Haouas*[a]*

AUTHOR ADDRESS

[a] Institut Lavoisier de Versailles (ILV), Université Paris-Saclay, UVSQ, CNRS, 78000, Versailles, France

[b] Institut des Sciences Moléculaires d'Orsay (ISMO), Université Paris-Saclay, CNRS, 91405, Orsay, France

[c] PHysicochimie des Electrolytes, Nanosystèmes InterfaciauX (PHENIX), Sorbonne Université, CNRS, 75252, Paris, France

[d] Current Address: CortecNet, 91940 Les Ulis, France

CORRESPODING AUTHORS:

Mohamed Haouas: mohamed.haouas@uvsq.fr

Anne-Laure Rollet: anne-laure.rollet@sorbonne-universite.fr

Ruxandra Gref: ruxandra.gref@universite-paris-saclay.fr

KEYWORDS. Degradation mechanism, Nanocarriers, Drug delivery, Metal-organic framework, Metal(III) phosphate, X-ray photoelectron spectroscopy, Small-angle X-ray scattering, NMR relaxometry

ABSTRACT. To make a drug work better, the active substance can be incorporated into a vehicle for optimal protection and control of drug delivery time and space. For making the drug carrier, the porous metal-organic framework (MOF) can offer high drug loading capacity, various designs for effective drug delivery performance, biocompatibility, and biodegradability. Nevertheless, its degradation process is complex and not easily predictable, and the toxicity concern related to the MOF degradation products remains a challenge for their clinical translation. Here, we describe an in-depth molecular and nanoscale degradation mechanism of aluminum- and iron-based nanoMIL-100 materials exposed to phosphate buffer saline (PBS). Using a combination of analytical tools, including X-ray photoelectron spectroscopy (XPS), nuclear magnetic resonance (NMR) spectroscopy, small-angle X-ray scattering (SAXS), and electron microscopy, we demonstrate qualitatively and quantitatively the formation of new coordination bond between metal(III) and phosphate, trimesate release, and correlation between these two processes. Moreover, the extent of material erosion, i.e., bulk or surface erosion, was examined from the transformation of nanoparticles' surface, morphology, and interaction with water. Similar analyses show the impact of drug loading and surface coating on nanoMIL-100 degradation and drug release as a function of metal-ligand binding strength. Our results indicate how the chemistry of nanoMIL-100(Al) and nanoMIL-100(Fe) drug carriers affect their degradation behaviors in a simulated physiological medium. This difference in behavior between the two nanoMIL-100s enables us to correlate better the nanoscale and atomic scale mechanisms of the observed phenomena, thus validating the presented multi-scale approach.

1. INTRODUCTION

The ongoing quest to search for the right drug delivery system (DDS) for the leading death causes and the blooming of nanotechnology in the 21st century have resulted in an ever-expanding library of drug carriers. One of the most recent materials for DDS is metal-organic framework (MOF), a coordination network between metals and organic ligands in a fashion that creates large voids in MOF structure.[1–3] This extraordinary porosity gives MOF the ability to adsorb a large amount of drug in a small amount of carrier. Therefore, the amount of foreign materials that need to be administrated to the patient decreases, potentially reducing the treatment's unwanted side effects. Additionally, MOF's diverse chemistry from its organic and inorganic counterparts allows for tunable functionalities for drug delivery.[4–6] As a result of these two advantages, MOFs reported in the literature have high payloads for a wide variety of active pharmaceutical ingredients (APIs),[7–9] and have been applied to treat various diseases.[10–12] Multiple drug loading and surface modification strategies have been developed. Nevertheless, due to the coordinative nature of their chemical bonds, the MOFs' *in vivo* applications have faced the challenge of unpredictable and non-generalizable degradation behaviors and associated toxicity.[13–16] Therefore, each type of MOF needs individual analysis of the degradation mechanism and nature of degradation products.

The MOF of our interest is chosen among the most studied for drug delivery,[13,17,18] the MIL-100 (MIL = Matériaux de l'Institut Lavoisier de Versailles).[19–21] The MIL-100 structure (**Figure 1**) is comprised of trivalent metal cations M(III) such as Al(III), Fe(III), and Cr(III), and tridentate ligands benzene-1,3,5-tricarboxylate, also called trimesate or BTC.[22–24] The MIL-100 secondary building unit (SBU) is the 6-fold coordinated trimer of M(III) with BTC, water, and hydroxyl. Its MTN framework has two types of mesopores: i) 29 Å diameter cages accessible through hexagonal (8.6 Å) and pentagonal windows (4.8-5.5 Å), and ii) 25 Å diameter cages accessible through

pentagonal windows. MIL-100 has several advantages as a drug vehicle. First, the big cages and large pore windows of MIL-100 benefit the penetration and adsorption of active molecules, leading to high drug payload and encapsulation efficiency. Second, their surface contains coordinative unsaturated sites (CUS) that can create several types of binding and interaction with active molecules, leading to controlled drug release.

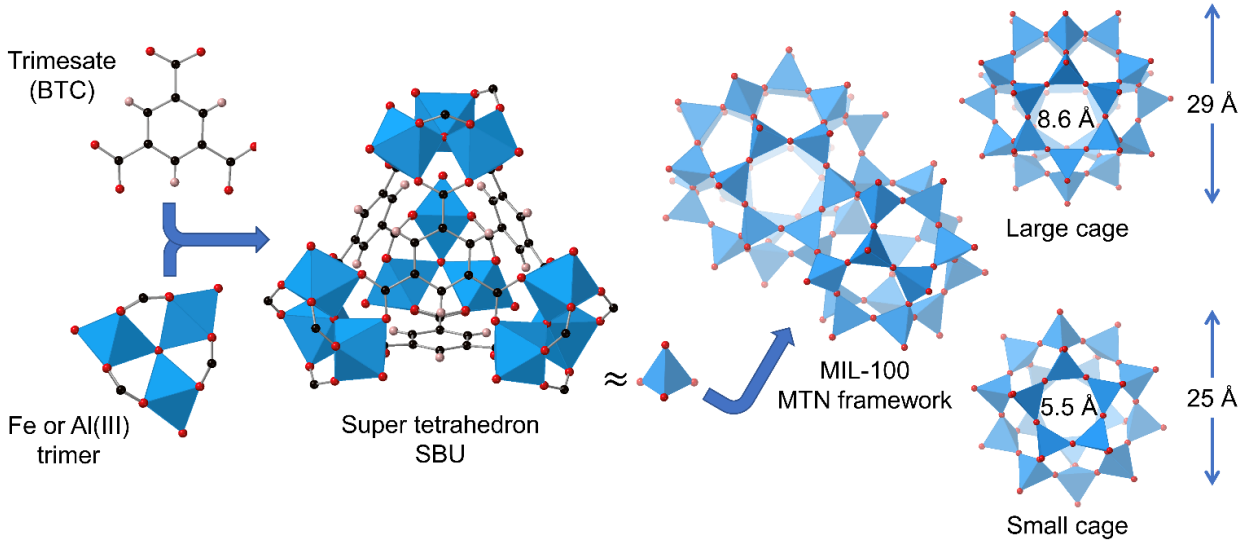

Figure 1. Structure of the MOF family MIL-100, constituted of M(III) trimer and trimesate ligands (BTC). The SBU of MIL-100 contains three metal cations M(III) coordinated with one central bridging oxygen and six carboxylate groups from several trimesate ligands. The 6-fold coordination sphere is completed with two water ligands and one hydroxyl group. Every four SBUs interconnected through trimesate ligands serve as the nodes of a tetrahedron. These tetrahedra are the nodes of the MTN framework of MIL-100 with two types of mesopores: i) 29 Å diameter cage accessible through hexagonal (8.6 Å) and pentagonal windows (4.8-5.5 Å), and ii) 25 Å diameter cages accessible through pentagonal windows.

In the MIL-100 family, nanoMIL-100(Fe) is the most popular DDSs. Its high drug loading capacity and controlled drug release have been demonstrated for numerous active compounds, including anti-cancer,[25,26] anti-retroviral,[27] anti-biotic,[28] and anti-inflammatory.[29] In addition to the structural advantages of the MIL-100 MOF, MIL-100(Fe) is made of endogenous iron. A pioneering *in vivo* study found no immune or inflammatory reactions over three months after injecting high doses (110-220 $mg.kg^{-1}$) of nanoMIL-100(Fe) in Wistar rats.[30] Eventually, the nanoMIL-100(Fe) degraded, and trimesate and iron were progressively eliminated from the body.

Likewise, nanoMIL-100(Al), the aluminum structural analog of MIL-100(Fe), has shown potential in drug delivery applications. Feng et al. described a MIL-100(Al) gel with a 62 wt% payload for the anti-cancer drug doxorubicin (DOX).[31] In another example, nanoMIL-100(Al) coated with γ-cyclodextrin-citrate DOX showed 74% efficiency for DOX encapsulation and controlled DOX release depending on the theoretical drug loading.[32] NanoMIL-100(Al) was also biocompatible *in vitro* and did not induce cell toxicity in several lung and liver cell lines.[33]

Both nanoMIL-100(Al) and nanoMIL-100(Fe) have exhibited specific interactions with phosphate-containing molecules.[34,35] This affinity towards phosphate has been employed to achieve a high drug payload and stable coating for nanoMIL-100. For example, gemcitabine monophosphate (Gem-MP) was loaded up to about 30 wt% with more than 98% efficiency, in contrast with less than 1 wt% of non-modified Gem.[25] Similarly, non-modified azidothymidine (AZT) was poorly incorporated in nanoMIL-100(Fe),[18,36] whereas the monophosphate and triphosphate derivatives of AZT (AZT-MP and AZT-TP, respectively) were incorporated up to around 36 and 25 wt%, respectively. The authors also found a stronger binding with Fe(III) of AZT-TP than AZT-MP. Our previous studies evidenced the existence of the coordination Al-O-P bond between adenosine triphosphate (ATP) and MIL-100(Al) and between the surface Al(III) and

phosphate-cyclodextrin (CDP),[32,37] which explains the successful incorporation of phosphate-functionalized molecules in nanoMIL-100 carriers.

However, this strong interaction with phosphate also causes the degradation of nanoMIL-100 at high phosphate concentrations. As phosphate ions are present in human bodies in non-negligible amounts, it is important to study their interactions with nanoMIL-100 analogs. Despite the abundant literature on drug loading and release, only some studies have addressed the critical topic of the nanoMIL-100 degradation mechanism. Several investigations pointed out that cell medium containing phosphate salts causes MIL-100(Fe) degradation, commonly believed to produce iron(III) derivatives and trimesic acid.[27,28,38] The release of trimesic acid was not observed in other simulated physiological media that do not contain phosphate salts. Moreover, Li et al. reported that upon incubation in phosphate buffer, the MIL-100(Fe) nano- and micro-particles lost 30% of their trimesate content but maintained their morphologies.[39] Based on the data of Raman, Mössbauer, and IR spectroscopy, the authors hypothesized the formation of an amorphous shell of iron phosphate and/or iron (hydr)oxide surrounding an intact crystalline core. Using *in situ* atomic force microscopy and high-resolution transmission electron microscopy, Christodoulou et al. also found that the nanoMIL-100(Fe) and microMIL-100(Fe) degraded without collapsing or changing their dimensions.[40]

Our recent study reported for the first time the atomic-scale structure of degraded nanoMIL-100(Al) and nanoMIL-100(Fe), evidenced by solid-state NMR and XANES spectroscopy, revealing a stepwise reaction process.[41] We also demonstrated the evolution of metal coordination structure for ATP-loaded and CDP-coated nanoMIL-100(Al). Nevertheless, we have yet to prove whether our proposed mechanism is generalizable to nanoMIL-100 DDSs. Different chemistry between iron and aluminum-based MIL-100 can play a role in their degradation and drug release

mechanisms. For example, the iron-trimesate MOF shows slightly better loading capacity towards DOX than the aluminum-trimesate.[32] Other authors found that nanoMIL-100(Al) degraded in modified Eagle cell culture medium, while nanoMIL-100(Fe) did not.[33]

Herein, we present a comparative study on the degradation and erosion mechanism of two structural analogs, nanoMIL-100(Al) and nanoMIL-100(Fe) DDSs. An array of complementary techniques is chosen to evaluate from the molecular to the nanoscale the evolution in the structure, composition, and morphology of nanoMIL-100(Al) and nanoMIL-100(Fe) upon their degradation by phosphate. In addition to pertinent MOF characterization techniques, X-ray photoelectron spectroscopy (XPS) was used to examine the chemical environment at the nanoMOF surface. Small-angle X-ray scattering (SAXS) and NMR relaxometry were used to probe the degradation and interactions of MOF nanoparticles with drugs and coatings in their suspension. Furthermore, we compared different host–guest interactions and influences on nanoMIL-100 degradation of two active compounds, ATP and adenosine monophosphate (AMP). The obtained qualitative and quantitative data provide a comprehensive view of the degradation and erosion process of nanoMIL-100 drug carriers.

2. EXPERIMENTAL METHODS

Detailed procedures, including synthesis and characterization of nanoMIL-100 materials, are given in the Supporting Information (SI).

2.1.Drug Encapsulation and Drug Release

Following a reported soaking procedure,[16,18] 5 mg.mL^{-1} MOF suspension was mixed with 1.25 or 1.5 mg.mL-1 drug aqueous solution of ATP or AMP, corresponding to 25 or 30 wt% input drug loading, respectively. Other experimental conditions were also used (see SI). The actual drug

payload wt% was calculated as: $\frac{m_{drug\ input} - m_{drug\ remaining}}{m_{MOF}} \times 100$, where $m_{drug\ input}$ is the weight of the drug added to nanoMOF. The amount of drug remaining in the supernatant after drug loading, $m_{drug\ remaining}$, was determined using HPLC or liquid NMR spectroscopy. The encapsulation efficiency (EE%) was calculated as the ratio between the actual loaded and the input drug quantities.

2.2.Surface Modification

Based on the method reported by Agostoni et al.,[42] nanoMIL-100 surface was coated with cyclodextrin phosphate (CDP) by mixing a MOF suspension of 10 mg.mL^{-1} with a CDP aqueous solution of 3 mg.mL^{-1}. CDP solution was prepared from β-CDP sodium salt (average 3-4 phosphate groups per cyclodextrin unit).

2.3.Degradation of NanoMIL-100

Original, drug-loaded, and surface-coated nanoMOF were suspended in phosphate buffer saline (PBS) pH 7.4 at 37 °C for 2-5 days under several conditions defined by nanoMOF and PBS concentrations (see Table S1). The molar ratios between PBS's phosphate and MOF's metal (P/M) were approximately 0.3, 0.5, 5.5, and 11.0. PBS was prepared from Dulbecco's Phosphate Buffered Saline (PBS) 1X, i.e., 10 mM, pH 7.0-7.3 (Gibco by life of Thermo Fisher), comprised of 8.1 mM Na_2HPO_4, 1.5 mM KH_2PO_4, 138 mM NaCl, and 2.7 mM KCl. After specific mixing durations, the degraded nanoMOF suspension was centrifuged and separated into the "degraded supernatant" and "degraded pellet" for *ex situ* analysis.

2.4.Characterization Methods

Morphology and size of 0.5 mg.mL^{-1} nanoMOF suspension were observed by scanning electron microscopy (SEM) under a 15 kV JEOL JSM-7001F microscope. A 40-50 μL sample was deposited on a silicon wafer and then metalized with a 5 nm-thick gold film. Energy-dispersive X-

ray spectroscopy (EDS) coupled with SEM, using a detector from Oxford Instruments, was employed to analyze the elemental composition of MOF.

High-performance liquid chromatography (HPLC) and liquid NMR spectroscopy were used to determine the amount of trimesate formed during nanoMIL-100 degradation and the amount of ATP/AMP after drug loading and drug release.

X-ray photoelectron spectroscopy (XPS) experiments on nanoMOF were conducted to study the chemical structure at the nanoMOF surface. Droplets (40-50 µl) of 10 $mg.mL^{-1}$ nanoMOF aqueous suspensions were deposited on a silicon wafer and dried before XPS measurement. High-energy-resolution core level spectra of C 1s, Al 2p, Fe 2p, and P 2p were deconvoluted for quantitative analysis.

The nanoMIL-100(Al) coordination structure was analyzed by solid-state NMR spectroscopy (ssNMR). All ssNMR spectra were measured at 11.7 T on a Bruker NEO NMR WB spectrometer equipped with probe heads of 3.2 mm, except the ^{31}P-^{27}Al 2D spectra that were recorded at 17.6 T on a Bruker Avance III WB NMR spectrometer with a 4 mm probe head (see experimental parameters in Table S2). The chemical shifts were referenced to tetramethylsilane for ^{1}H and ^{13}C, $Al(NO_3)_3$ 1 $mol.L^{-1}$ solution for ^{27}Al, and H_3PO_4 85 wt% solution for ^{31}P.

SAXS experiments were conducted at the SWING beamline (Synchrotron SOLEIL, France) to monitor the morphological evolution of MIL-100 nanoparticles (NPs). NanoMOF suspension of 10 $mg.mL^{-1}$ was inserted in cylindrical glass capillaries of 1 mm outer diameter, which was then sealed by flame.

NMR relaxometry was conducted using a fast-field-cycling (FFC) relaxometer from Stelar, which measures the ^{1}H longitudinal relaxation rates ($R_1 = T_1^{-1}$) when varying the ^{1}H Larmor frequency. The measurement outcome, the Nuclear Magnetic Relaxation Dispersion (NMRD)

profile, plots the relaxation rate R_1 versus the NMR frequency. The SpinMaster relaxometer probes the low-frequency domain from 10 kHz to 30 MHz. T_1 has been measured using a pre-polarized sequence from 10 kHz to 10 MHz and a non-polarized sequence from 10 MHz to 30 MHz.

3. RESULTS AND DISCUSSIONS

NanoMIL-100(Al) and nanoMIl-100(Fe) were obtained by microwave synthesis, adapting published procedures.[43] The prepared nanoMIL-100(Al) and nanoMIL-100(Fe) suspensions showed similar particle size, chemical composition, crystal structure, and porosity. However, we observed a significant difference in their colloidal stability in water (see SI, Figure S1-S9, Tables S3-S6).

3.1. Degradation Mechanisms of Original NanoMIL-100(Al) and NanoMIL-100(Fe) at Molecular Scale

The degradation mechanism of nanoMIL-100(Al) and nanoMIL-100(Fe) in PBS were compared by probing modification in their molecular structure in an *ex situ* manner. After incubating nanoMOF in PBS at 37 °C for specific periods, the suspension was centrifuged to recover "degraded supernatant" and "degraded pellet'', containing the liquid and solid degradation products, respectively. These recovered products were analyzed by a set of complementary methods.

3.1.1. Degradation kinetics in the liquid phase.

Released trimesate was detected in the nanoMIL-100's liquid degradation media by lqNMR spectroscopy. The ^{1}H NMR spectra of the degraded supernatant contain the signature of aromatic proton peaks of trimesate/trimesic acid in the region 8.3-8.5 ppm (Figure S10), indicating the formation of free ligand upon nanoMOF degradation. The kinetics of trimesate release was thus

quantified and plotted in Figure 2. Different nanoMOF and PBS concentrations were used to vary phosphate-to-metal molar ratios (P/M, where M is Fe or Al). Globally, the profiles of trimesate release from both nanoMIL-100 consist of two stages: i) a fast stage in the first three hours after incubation in PBS and ii) a subsequent gradual stage until the equilibrium is reached after around 24 h. Other authors, including us, also found this time-dependent release pattern.[27,28,40,41] In this investigation, we demonstrate that the phosphate-to-metal molar ratio (P/M) directly influences the extent of nanoMIL-100 degradation. When incubating nanoMIL-100 in DI water with no phosphate, a negligible amount of trimesate was detected by lqNMR, less than 2% in the case of nanoMIL-100(Al) and non-observable for nanoMIL-100(Fe). In contrast, when phosphate is present in the medium (Figure 2), the higher the P/M ratio, the higher the amounts of released trimesate from both nanoMIL-100(Fe) and nanoMIL-100(Al). Notably, nanoMIL-100(Al) showed a higher magnitude of % trimesate release, hence the magnitude of degradation than nanoMIL-100(Fe). For example, at a very low P/M ratio (0.3), trimesate release from nanoMIL-100(Al) was nearly twice as much as that from nanoMIL-100(Fe) (31% and 15%, respectively). Also, the iron-

based MIL-100 has a more progressive profile of trimesate formation than its aluminum analog, especially at a high degradation ratio P/M.

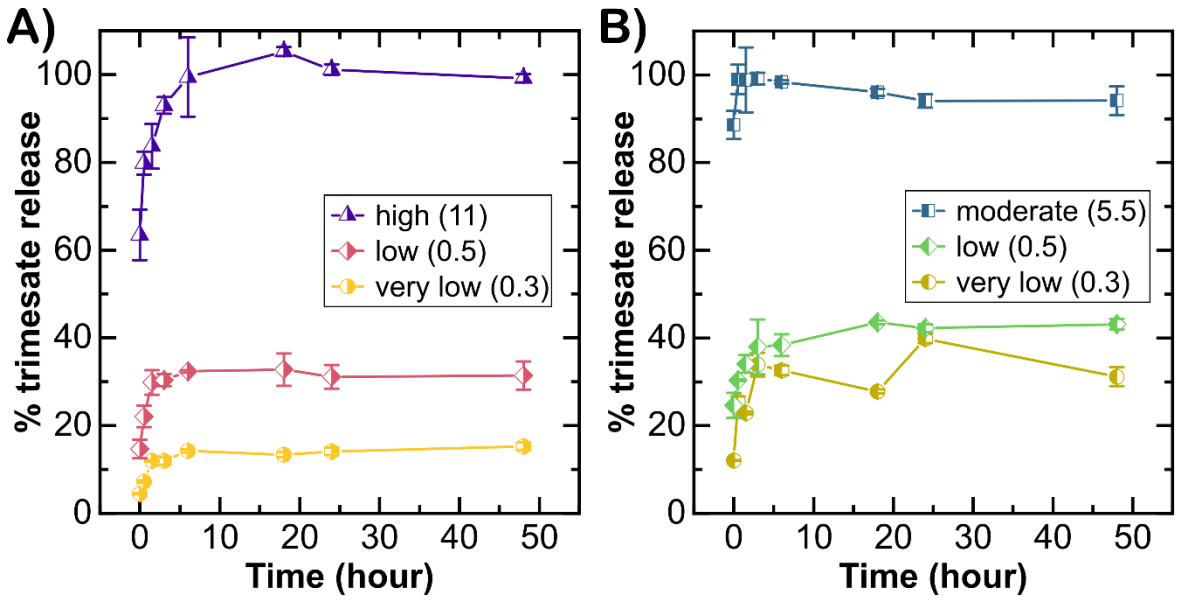

Figure 2. Kinetics of trimesate release from degradation of (A) nanoMIL-100(Fe) and (B) nanoMIL-100(Al). Several phosphate-to-metal (P/M) molar ratios, calculated from PBS and nanoMOF concentrations, were used, namely very low (0.3), low (0.5), moderate (5.5), and high (11).

The apparent first-order kinetics in trimesate release could be due to insufficient phosphate in the degradation media to react with nanoMIL-100. The higher the P/M ratio, the higher the trimesate release. Also, the lower the P/M ratio, the more phosphate was consumed. When the P/M ratio was raised from 0.3 to 0.5, the consumed amount of phosphate dropped from 83% to 35%, as indicated in the ^{31}P NMR spectra of nanoMIL-100(Al)'s degraded supernatant (Figure S11). However, phosphate was still present in the degradation medium while less than 100% trimesate was released, which argues for a more complex equilibrium mechanism preventing the reaction from proceeding further.

Briefly, the quantitative liquid NMR spectroscopy data unambiguously evidence the correlation between the amount of phosphate in the media and the trimesate release from nanoMIL-100 frameworks. Therefore, phosphate inorganic ions in PBS are directly involved in the nanoMIL-100 degradation. This degradation process will directly influence and dictate the drug delivery mechanism, as demonstrated below (see section **3.2 Degradation and Drug Release**).

3.1.2. Changes in crystallinity, porosity, and functional group.

The solid-phase reaction products were characterized to understand the mechanisms behind MIL-100 degradation. Several reaction times were used to assess the time evolution of the reaction with several P/M ratios, e.g., 0.3, 0.5, and 11. Equilibrium was reached after 48 h incubation in PBS for all P/M ratios.

First, PXRD suggests that nanoMIL-100 kept its long-range crystal structure after degradation. In Figure S12, the XRD pattern of 48 h degraded nanoMIL-100(Al) at low P/Al ratio did not differ much from the parent sample despite a non-negligible loss of 42% initial trimesate content (see Figure 2B). However, the same degraded nanoMIL-100 underwent a dramatic porosity reduction. The N_2 uptake of degraded nanoMIL-100(Al) and nanoMIL-100(Fe) remarkably decreased (Figure S13). The BET surface areas decreased from 1632 and 1621 $m^2.g^{-1}$ to 228 and 973 $m^2.g^{-1}$, respectively. Assuming the inner cage structure is intact after MOF degradation, possible reasons are restricted access to the MOF pores and/or reduced pore volume and internal surface area due to trapped species inside the pore.

The functional groups of nanoMIL-100 were also modified upon its degradation. IR spectroscopy measurement on degraded nanoMIL-100(Al) and nanoMIL-100(Fe) showed increasing Al-O-P and Fe-O-P broad vibration bands at 1089 and 1022 cm^{-1}, respectively, as a function of degradation time (Figure S14). Still, the IR fingerprints of trimesate, e.g., aromatic C-

H bands at 760-770 and 700-710 cm^{-1}, were present since nanoMIL-100(Al) and nanoMIL-100(Fe) lost at maximum 10% and 20% of their initial trimesate content, respectively.

3.1.3. Chemical environment and atomic composition at nanoMOF surface.

XPS was used to investigate the chemical environment at the nanoMOF surface, which is expectedly essential for any reaction of nanoparticles. The core-level XPS spectra of original nanoMIL-100(Al) and nanoMIL-100(Fe) shown in Figure S15 are consistent with the nanoMIL-100 structure. The reconstructed C 1s contains the contribution of C carboxylate and C aromatic C sp^2 at 288.5 and 284.6 eV, respectively. Also, the Al 2p and Fe 2p core levels spectra of MIL-100(Al) and MIL-100(Fe) have their peak shape and binding energy position consistent with a metal(+III) oxidation state and a metal-oxygen bonding.

XPS measurement of degraded nanoMIL-100 revealed considerable changes in its chemical environment and coordination sphere after degradation. First, the C 1s spectra of 48-hour-degraded nanoMIL-100 (Figure 3A-B) illustrate a decrease in the C 1s global intensity and the signals associated with trimesate carboxylate and C sp^2. These trimesate peaks even disappeared in the case of degraded nanoMIL-100(Al). Second, the P 2p core level spectrum (Figure S16) exhibits a doublet around 133 eV, characteristic of the phosphate ions. According to the low amount of Na (below 2%) and the absence of K in the survey spectra of degraded samples, phosphate cannot only come from the degradation medium PBS residues. Therefore, this P 2p peak represents the phosphate incorporated in the MIL-100 structure, possibly coordinating with the Al/Fe metal center in MIL-100 through the Al-O-P/Fe-O-P bond. Finally, the Al 2p and Fe 2p spectra of the degraded nanoMIL-100(Al) and nanoMIL-100(Fe) (Figure 3C-D) have binding energies similar to their corresponding original nanoMIL-100, indicating no significant change in these metals' oxidation state. The suspected transformation from M-O-C to M-O-P slightly affects the Al 2p and

Fe 2p binding energy. Regarding the degraded nanoMIL-100(Al), the broadening and the drift of the Al 2p peak might be associated with conductivity change.

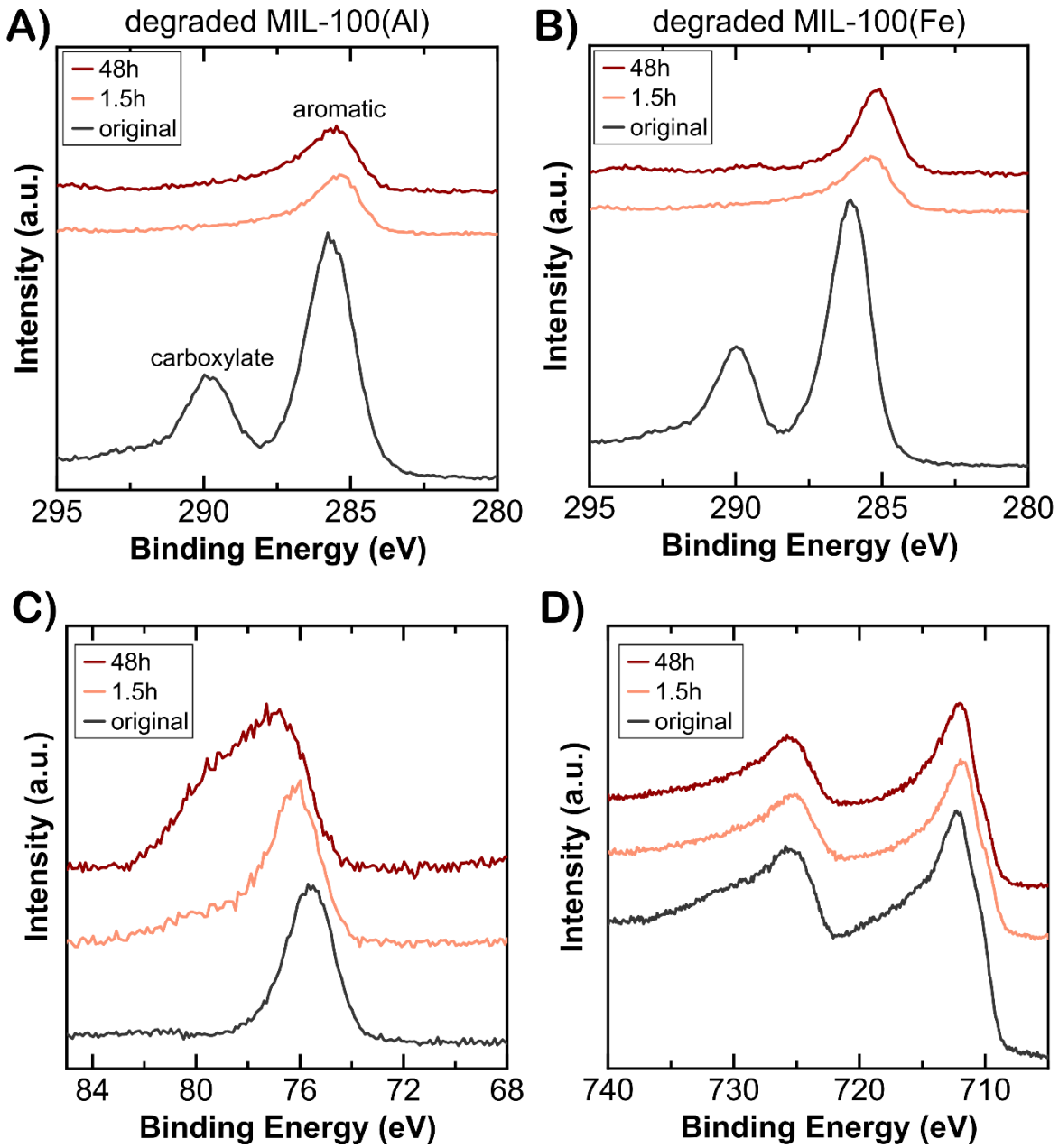

Figure 3. Time evolution of XPS spectra of (A, C) degraded nanoMIL-100(Al) and (B, D) nanoMIL-100(Fe) at high P/M ratio of 11: (A, B) C 1s, (C) Al 2p, and (D) Fe 2p core level.

The XPS data demonstrate the disappearance of trimesate ligands and the appearance of phosphate in the degraded MIL-100 pellets, which is entirely consistent with the increase of trimesate concentration and decrease of phosphate concentration in the degraded supernatant shown by lqNMR spectroscopy. Moreover, we can correlate the C/M (carbon-to-metal) and P/M (phosphorous-to-metal) ratios in the degraded pellets' surface (atomic composition obtained from XPS) and % trimesate release in the degraded supernatant (lqNMR data). Figure 4A shows a linear correlation between the decrease of the C/M ratio in the degraded solid and the increase of % trimesate release in the degraded liquid, evidencing the cleavage of trimesate ligand due to MOF degradation. Likewise, Figure 4B suggests a linear tendency between the increase of the P/M ratio and the increase in % trimesate release, indicating the incorporation/coordination of phosphate in the MIL-100 framework upon incubation in PBS. These two trends suggest that ligand substitution between trimesate and phosphate happens during nanoMIL-100's degradation reaction with PBS.

While the XPS technique provides atomic composition at the material's surface (5-10 nm deep), one can also estimate the atomic composition in the bulk material (1-2 μm deep) by EDS. The P/M ratio in the degraded solid determined by EDS is plotted versus the % trimesate release in Figure 4C. The magnitude of the P/M ratio determined by EDS is lower than that determined by XPS, as the reaction takes place more intensely at the surface than in bulk. An important observation from Figure 4C is that with a rising proportion of trimesate release, the bulk P/Al increases gradually. However, the bulk P/Fe ratio rises more slowly and seems to reach a limit when the % trimesate release approaches 100%. At a high level of trimesate release (60-80%), the bulk P/M ratio of degraded nanoMIL-100(Fe) is lower than its counterpart in degraded aluminum MOF. Possibly, the degradation reaction propagates deeper and takes place more uniformly in nanoMIL-100(Al) than in nanoMIL-100(Fe) particles. Conversely, the surface P/Fe ratio is higher and increases faster

than the surface P/Al ratio, indicating that the surface reaction was faster for the iron MOF than its aluminum analog.

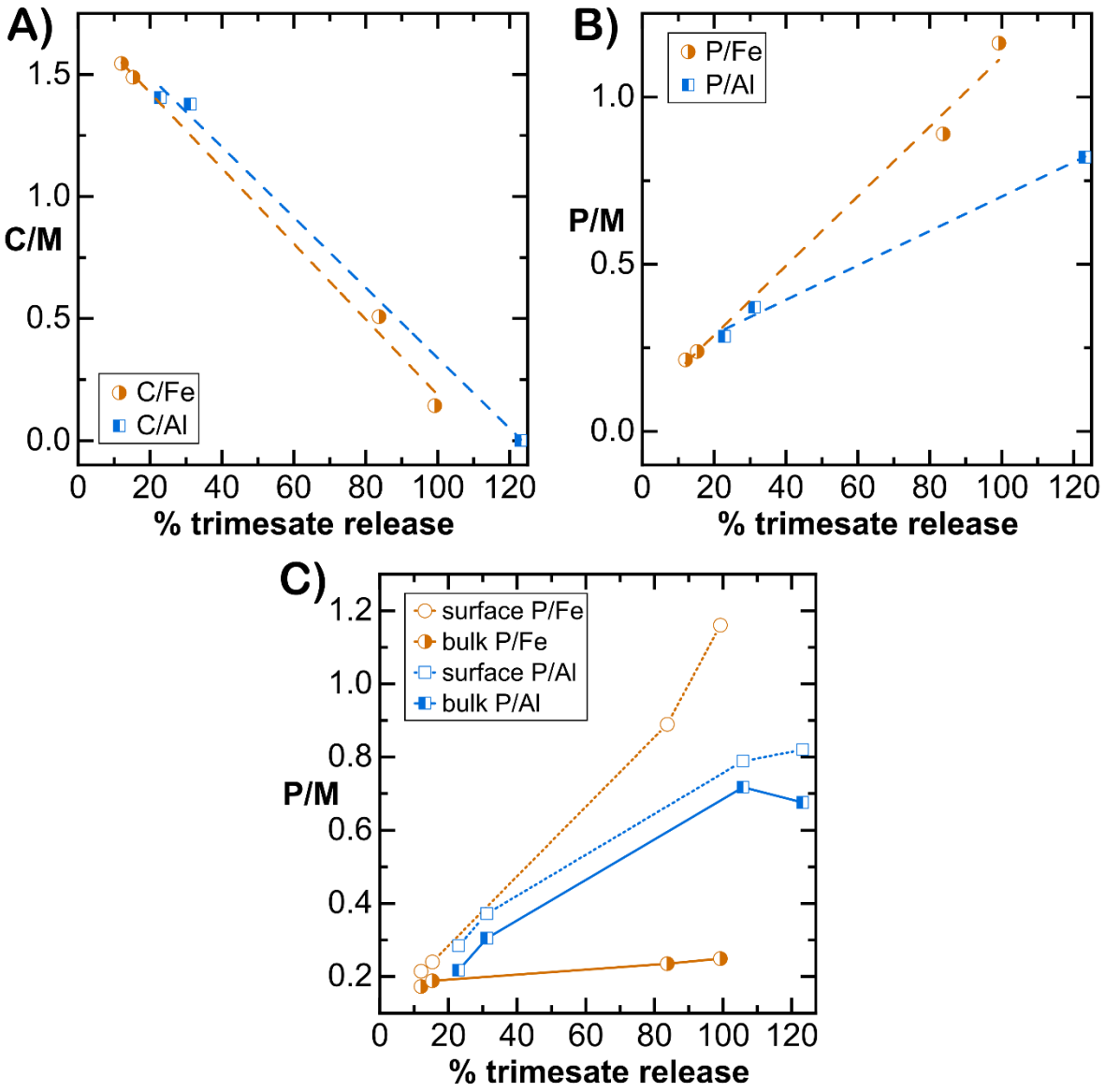

Figure 4. (A-B) Correlation between XPS atomic composition C/M and P/M ratio, respectively, vs. % trimesate release in degraded nanoMIL-100(Al) and nanoMIL-100(Fe). (C) Correlation between the P/M ratio determined by EDS (bulk) or by XPS (surface) and % trimesate release in degraded nanoMIL-100(Al) and nanoMIL-100(Fe). The estimated uncertainty of the quantification using XPS and EDS data is 10%.

The qualitative and quantitative data from lqNMR, XPS, and EDS reported here consolidate our published proofs for Al-O-P/Fe-O-P coordination bond in the degraded nanoMIL-100(Al)/nanoMIL-100(Fe) and proposal on ligand substitution reaction mechanism.[41] Furthermore, the current study illustrates that the two analogs nanoMIL-100 experience similar degradation reaction steps at the molecular scale but at different rates and extents. At pH 7.4, the phosphate buffer at equilibrium contains 61% of dibasic phosphate ions, i.e., monohydrogen phosphate HPO_4^{2-}, and 39% of monophosphate ions, i.e., dihydrogen phosphate $H_2PO_4^-$ (Figure S17). A previous study has shown MIL-100(Fe) was more stable at pH 5.4 than 7.4,[40] where the dihydrogen phosphate anion is the dominant species (98% $H_2PO_4^-$ and 2% HPO_4^{2-}). Therefore, the active species responsible for nanoMOF degradation at near neutral pH is more likely the monohydrogenphosphate anion HPO_4^{2-}, which can act as a nucleophilic substituting agent towards coordination complexes.[44] In the first reaction step, the HPO_4^{2-} anions of PBS substitutes the labile water ligands of nanoMIL-100 and coordinates with the Al/Fe(III) cations through M-O-P coordination bond (M = Al, Fe). Next, phosphate ions replace the carboxylate of MIL-100's trimesate ligands. When all six M-O-C bonds between a trimesate ligand and Al/Fe trimers are broken, free trimesic acid is formed and released into the solution. The main degradation products are aluminum phosphate/iron phosphate complex.

The two analogs, MIL-100(Al) and MIL-100(Fe), have similar degradation reaction steps but react with phosphate at different rates and extents. The trimesate release during nanoMIL-100(Al)'s degradation is faster and has a higher magnitude. The bulk P/M ratio in the degraded MIL-100(Al) pellet is also higher. Thus, it appears that nanoMIL-100(Al) is more prone to degradation by phosphate than its iron analog. This difference in reactivity can be explained by the metal-ligand binding strength between Al/Fe(III) and carboxylate/phosphate. Several authors have

reported that Fe(III) has a higher complexing affinity towards phosphate and several carboxylate ions than Al(III).[45,46] With respect to aluminum, iron cations favor bonding with phosphate and also bonding with trimesate. It is plausibly this push-and-pull affinity that makes the release of trimesate, hence making the degradation reaction of the iron MOF more progressive than that of the aluminum analog.

Different reactivity towards phosphate of Fe(III) and Al(III) might explain the reaction heterogeneity of nanoMIL-100 material. Since phosphates are more attracted to Fe(III) than Al(III), degradation initiates on the nanoMIL-100 surface faster for the iron-based nanoMOF than the aluminum-based one, leading to a higher surface P/Fe ratio than the P/Al ratio. Nonetheless, as the reaction continues and penetrates the NPs, the cleavage of trimesate was less favored in nanoMIL-100(Fe) than in nanoMIL-100(Al). Consequently, the bulk of nanoMIL-100(Al) is degraded more easily than that of nanoMIL-100(Fe), gradually increasing the bulk P/Al ratio. Unlike the homogenous degradation in nanoMIL-100(Al), the process is limited in the bulk nanoMIL-100(Fe), slowing down and limiting the increase in bulk P/Fe ratio.

3.2. Degradation and Drug Release with Modified NanoMIL-100(Al) and NanoMIL-100(Fe) at Molecular Scale.

In this section, we examine the impact of drug encapsulation on the nanoMIL-100(Al) and nanoMIL-100(Fe) degradation processes. Literature has shown that the presence of loaded active molecules can alter the physicochemical properties of nanoMOF,[42] thus potentially influencing its degradation reaction. Here, nanoMIL-100(Al) and (Fe) are loaded with ATP and AMP. Studying these two drugs belonging to the same family but with different numbers of phosphate functional groups could reveal the effect of metal-ligand complexation strength on drug delivery processes, including drug encapsulation, drug release, and carrier degradation.

First, the interaction of ATP and AMP with two nanoMOFs was compared by mixing them with different MOF and drug concentrations (the choice of MOF and drug concentration is explained in the SI). The obtained drug payload wt%, encapsulation efficiency (EE%), and % trimesate loss are given in Table S7 and S8 (see also Figure S18-S20). For ATP, no matter the input ATP loading wt% and MOF concentration, nanoMIL-100(Fe) always gave higher ATP payload and EE% (≈ 100%) than nanoMIL-100(Al). As Fe^{3+} cations create a more stable complex with triphosphate than Al^{3+} cations,[45] MIL-100(Fe) forms a more stable complex with triphosphate than MIL-100(Al), hence a higher affinity towards capturing ATP. Meanwhile, unlike ATP drug loading, the two nanoMIL-100 have close AMP drug payload and EE% values, hence similar affinity towards AMP.

Notably, a non-negligible amount of trimesate was detected in the supernatant recovered from the drug-loading suspension of nanoMIL-100 and ATP/AMP (Figure S19). The higher the input drug loading, the higher the %BTC loss is. At a given MOF concentration, the % trimesate loss upon AMP encapsulation (8-16%) is lower than upon ATP encapsulation (9-20%). As phosphate is more nucleophilic than the carboxylate group, ATP and AMP can act as nucleophilic substituting agents and replace trimesate ligands when mixing ATP/AMP with nanoMIL-100. AMP with one phosphate group interacts less with the metal cluster than ATP with three consecutive phosphate groups. Thus, at the same ATP/AMP concentration, AMP has a lower tendency to attack trimesate ligands.[47] Total maintenance of trimesate content, i.e., zero trimesate loss, likely requires very low input drug loading below 10 wt%,[36] which is not preferred in this case. Therefore, the chosen ATP/AMP loading formulation to compromise drug payload, EE%, and %BTC loss was 25 wt% input ATP and 5 $mg.mL^{-1}$ of nanoMIL-100.

The nature of the interaction between phosphate drugs ATP/AMP and nanoMIL-100 carrier was identified by solid-state NMR (ssNMR) experiments on nanoMIL-100(Al). We took advantage of ^{27}Al and ^{31}P NMR that give signals exclusively belonging to the MOF and the drug, respectively.

^{27}Al NMR spectroscopy demonstrates that the six-fold coordination mode of Al centers is kept upon drug loading (Figure 5A). A new broad shoulder around -10 ppm can be seen in the spectrum of ATP-loaded-nanoMIL-100(Al). These new 6-coordinate Al species in drug-loaded MIL-100(Al) are better observed in MQMAS spectra (Figure S21). Porcino et al. proved by ^{31}P-^{27}Al *D*-HMQC correlation NMR experiments that this new peak represents the Al coordinating bonded to the terminal γ-phosphate group of ATP through an Al-O-P coordination bond, resulting from the substitution of water ligand.[37] ^{31}P-^{27}Al *D*-HMQC NMR verified that a similar Al-O-P bonding exists in AMP-loaded-MIL-100(Al) (Figure 5B). Notice that in the 1D ^{27}Al NMR spectrum (Figure 5A), the new Al-6-coordinate resonance is more intense in ATP-loaded than in AMP-loaded nanoMIL-100(Al), indicating that the aluminum cluster interacts more strongly with ATP than with AMP.

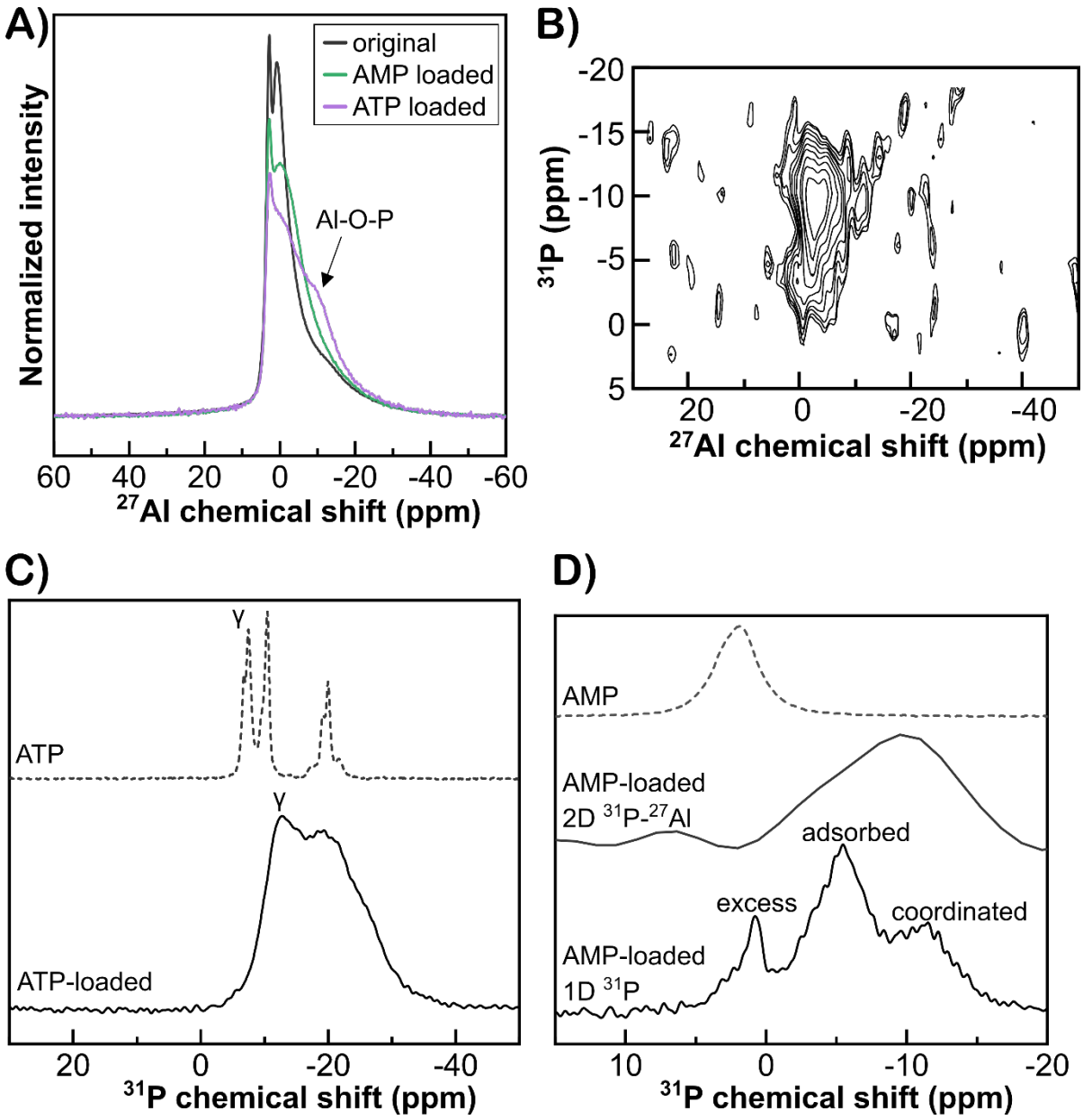

Figure 5. (A) 1D ^{27}Al MAS NMR spectra of the original and loaded MIL-100(Al) with ATP and AMP. (B) 2D ^{31}P-^{27}Al *D*-HMQC NMR spectrum. (C) ^{31}P NMR spectra of ATP and ATP-loaded nanoMIL-100(Al). (D) ^{31}P NMR spectra of AMP and AMP-loaded MOF compared to the ^{31}P dimension extract from its 2D ^{31}P-^{27}Al *D*-HMQC NMR spectrum.

Also, the chemical coordination between ATP and nanoMIL-100(Al) is proved by ^{31}P NMR spectroscopy. Figure 5C shows a significant shift and broadening of three peaks compared to pure ATP's spectrum due to chemical coordination between ATP and Al(III) through the terminal phosphate group (γ-P). The assignment of α-, β-, γ-P signals here was based on previously published ^{31}P-^{31}P DQ-SQ MAS NMR spectroscopy data.[37]

Contrasting to the triphosphate derivative ATP, pristine AMP comprises a single phosphate group, thus having only one ^{31}P NMR resonance at 1.9 ppm. However, three distinctive resonances were observed in the ^{31}P MAS NMR spectrum of AMP-loaded-nanoMIL-100(Al) (Figure 5D). The peak at 0.8 ppm is similar to pure AMP. Thus, it is assigned to the excess AMP, which is not incorporated in MIL-100 pores but assumably trapped at its external surface. This peak's assignment is also supported by ^{31}P-^{27}Al NMR measurement (Figure 5B), which shows that this phosphorous species does not correlate with any ^{27}Al resonance of MIL-100. Meanwhile, the two other phosphorous species, whose chemical shifts are at -5 and -12 ppm, exhibit correlations with ^{27}Al, proving their encapsulation in MOF cages. In the extraction from the 2D spectrum, the intensity of the ^{31}P peak at -12 ppm is much higher than the peak at -5 ppm (Figure 5D). Therefore, the ^{31}P peak at lower NMR chemical shift is assigned to AMP coordinated to Al of MIL-100(Al) framework because the deshielding effect should manifest more on the P atom chemically bonded to Al. The ^{31}P peak at -5 ppm is associated with AMP adsorbed physically in the pores but not chemically bonded to the framework.

More importantly, the interactions of ATP and AMP with nanoMIL-100 influence the nanoMIL-100 carrier degradation. Figure 6A-B shows that compared to the non-loaded counterpart, trimesate release from ATP-loaded nanoMIL-100 is lower, while trimesate release from AMP-loaded nanoMIL-100 is comparable. This impact of drug loading on the degradation process is

particularly true for iron nanoMOF. At the same time, not much can be seen for aluminum analog, highlighting the difference in affinity of phosphate ligands (organic or mineral) towards iron and aluminum cations. As previously shown, ATP with the triphosphate group has a more robust interaction with nanoMIL-100 than AMP with the monophosphate group. Thus, the loaded ATP has a more pronounced effect on nanoMIL-100 degradation than AMP. Also, AMP is released faster from nanoMIL-100 carrier than ATP (Figure 6C-D).

In addition, upon drug release in PBS, nanoMIL-100(Al) and (Fe) continue to exhibit different reactivity of metal cations. Notice from Figure 6A-B that trimesate is released more slowly and gradually from drug-loaded MIL-100(Fe) than from drug-loaded MIL-100(Al). Likewise, in Figure 6C-D, the drug release process of ATP and AMP from nanoMIL-100(Fe) is more progressive than from nanoMIL-100(Al). This more controlled behavior of iron MOF is already observed when no drug is loaded. In addition, the difference between ATP release patterns from the two MOFs (Figure 6C) is more significant than between AMP release patterns (Figure 6D). This observation agrees with the fact that MIL-100(Fe) has a higher affinity towards ATP than MIL-100(Al), while they share a similar affinity towards AMP.

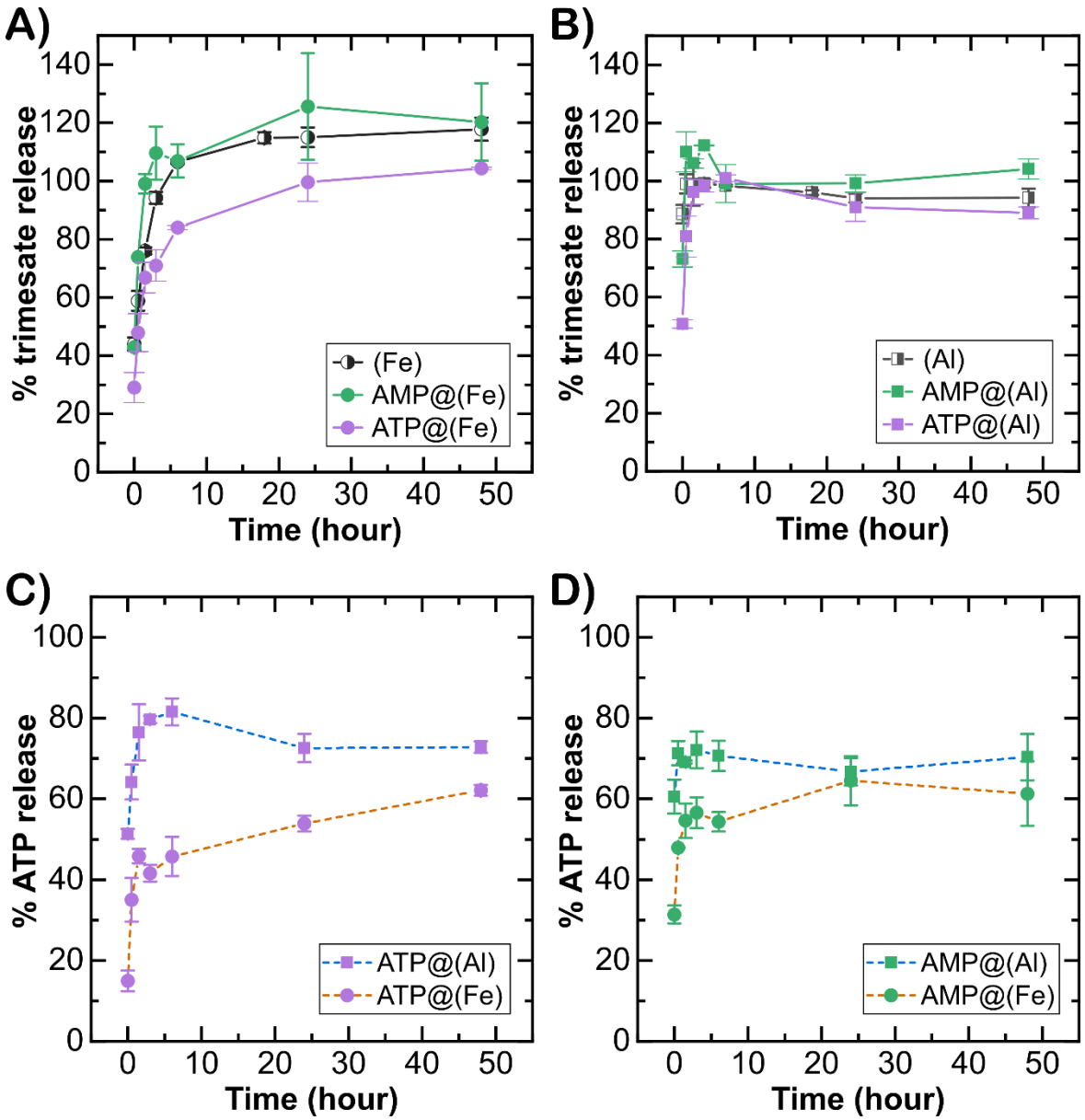

Figure 6. (A-B) Kinetics of trimesate release from degradation of non-loaded, ATP-loaded, and AMP-loaded MOFs: (A) nanoMIL-100(Fe), and (B) nanoMIL-100(Al). (C-D) Kinetics of (C) ATP and (B) AMP drug release from the degradation of drug-loaded nanoMIL-100(Fe) and nanoMIL-100(Al). The degradation P/M ratio of 5.5 was used.

Insights into the relation between trimesate and drug release were provided by ssNMR spectroscopy, following our previous method.[41] Degradation of the AMP-loaded nanoMIL-100(Al) behaves like the degradation of the original one. Its ^{27}Al MAS NMR spectrum (Figure 7A) displays the signal around -5 ppm characteristic of 6-coordinate Al-O-P between MIL-100(Al) and PBS. It also shows the peak of 4-coordinate Al at 48 ppm (Figure 7B). Also, the ^{31}P MAS NMR spectrum (Figure S22B) indicates an increased signal intensity at -11 ppm, a similar position to the phosphate from PBS coordinated to the framework Al. On the contrary, the degradation of the ATP-loaded nanoMIL-100(Al) has distinctive features. The ^{27}Al NMR shows no detectable sign of low-coordinate Al (Figure 7B). The main degraded species is still the 6-coordinate Al coordinated with PBS around -2 ppm. The ^{31}P MAS NMR spectrum in Figure S22A shows the peak of coordinated PBS phosphate and the contribution of unreleased ATP.

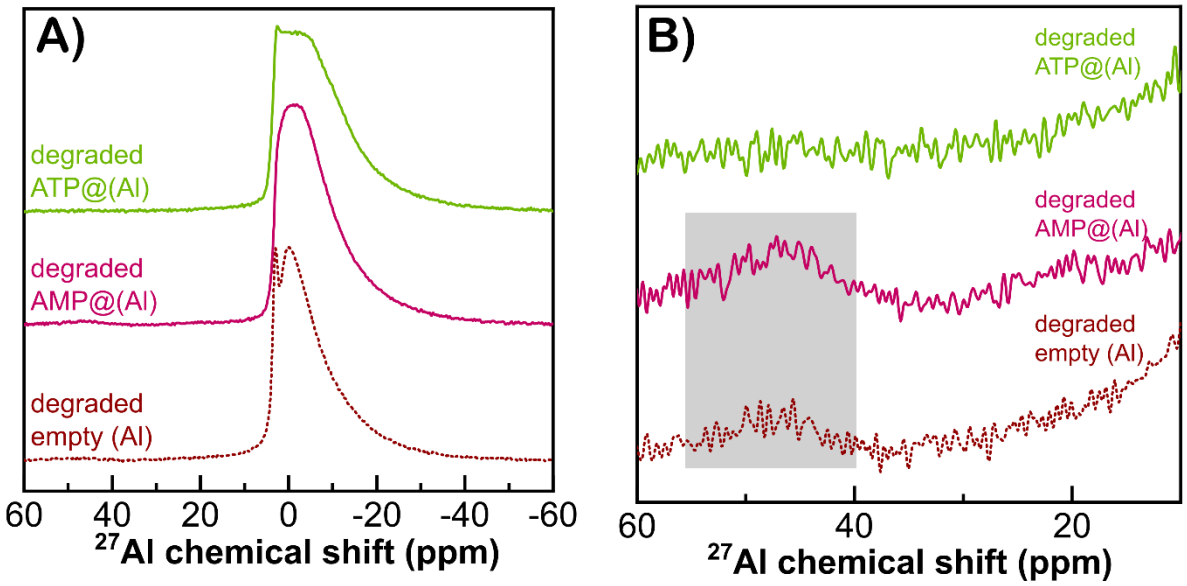

Figure 7. (A) ^{27}Al MAS NMR spectra of degraded original and drug-loaded MIL-100(Al), and (B) zoom on chemical shift region of 4- and 5-coordinate Al. The degradation P/Al ratio was 0.3, and the duration was 48 hours

Both containing monophosphate groups, AMP and PBS, have comparable binding strength with Al cations. It was reported that AMP and HPO_4^{2-} have similar metal complex formation constant values.[48] Therefore, they compete to coordinate the MIL-100 framework's Al cations. Once PBS replaces the labile water ligands, as trimesate ligand has weaker binding strength with Al than AMP and PBS, the Al-O-C bonds with trimesate are weakened and probably broken first. When more and more 6-coordinate Al-O-PBS are formed, the coordination bond Al-O-AMP is weakened. Then PBS can easily replace the coordinated AMP, leading to AMP release. The drug will be totally released when phosphate ions substitute all coordinated AMP. The main degradation products of AMP-loaded nanoMIL-100(Al) are 6-coordinate aluminum phosphate, free trimesate, and free AMP. The 4-coordinate Al species could be formed as a side product during Al-O-trimesate and Al-O-AMP bond dissociation.

Meanwhile, both ^{27}Al and ^{31}P NMR data suggest that nanoMIL-100(Al) loaded with ATP is less degraded than the one loaded with AMP, in agreement with the quantitative data of drug release and trimesate release. The triphosphate ATP is a much stronger complexing ligand towards metal(III) cations than AMP; thus, breaking the coordination between ATP and Al(III) is more difficult. As we hypothesized,[41] PBS probably attacks the Al-O-C bond with trimesate first, forming 6-coordinate Al-O-P observed at -2 to -5 ppm in the ^{27}Al NMR spectrum. Then, ATP is substituted by PBS and released from MIL-100(Al). Bulky ATP could hinder phosphate diffusion into the MIL-100(Al) cage, limiting trimesate substitution and ATP release. As a result, ATP release is slower than AMP release. Additionally, the notable absence of the 4-coordinate aluminophosphate when degrading ATP-loaded MOF at the very low P/Al ratio could be due to the competition between the β-phosphorus of ATP and phosphate PBS ions to coordinate with dangling Al(III) cations.[49,50]

3.3.Degradation Process of NanoMIL-100(Al) and NanoMIL-100(Fe) at Nanoscale

As demonstrated in this study, nanoMIL-100(Al) and nanoMIL-100(Fe) suspensions have different colloidal stability. Thus, the degradation of these NPs might occur differently at the nanoscopic scale.

3.3.1. Changes in particle morphology.

Small-angle X-ray scattering (SAXS) was selected to follow the evolution of the nanoscopic features of nanoMIL-100(Al) and nanoMIL-100(Fe) suspension during their degradation reaction. SAXS allows looking into the colloidal state in the suspension phase, such as particle size and aggregation. In our experiments conducted in synchrotron (details in SI), the correlation distance range spans roughly from 3 to 300 nm, calculated from π/q, where q is the scattering vector in $Å^{-1}$. In addition, electronic microscopy experiments were performed to complement the X-ray scattering data.

SAXS curves of the original nanoMIL-100 suspension in ethanol and deionized water are presented in Figure 8. The first difference lies at low q, where the scattering pattern of iron MOF is smooth while the one of aluminum MOF is bent around q of 0.005 $Å^{-1}$. This first cross-over corresponds to the mean particle size of nanoMIL-100(Al) in water, approximately 60 nm.[51] The q^{-2} slope below 0.005 $Å^{-1}$ shows that the particles are not isolated but aggregate, consistent with DLS and TEM measurements of nanoMIL-100(Al) in water (see Table S3 and Figure S5). The nanoMIL-100(Fe) size is slightly larger, and the corresponding cross-over expected at lower q values was not detected in the present SAXS configuration. Nevertheless, the curvature observed at very low q can be associated with particle size. The second difference between the two nanoMIL-100 was found in the 0.02-0.1 $Å^{-1}$ q range in the Porod regime, where a slight upward tail starting from q 0.05 $Å^{-1}$ was observed for nanoMIL-100(Fe) and not for nanoMIL-100(Al).

This feature of nanoMIL-100(Fe)'s SAXS pattern could be associated with a modified particle interface or an additional diffuse scattering.

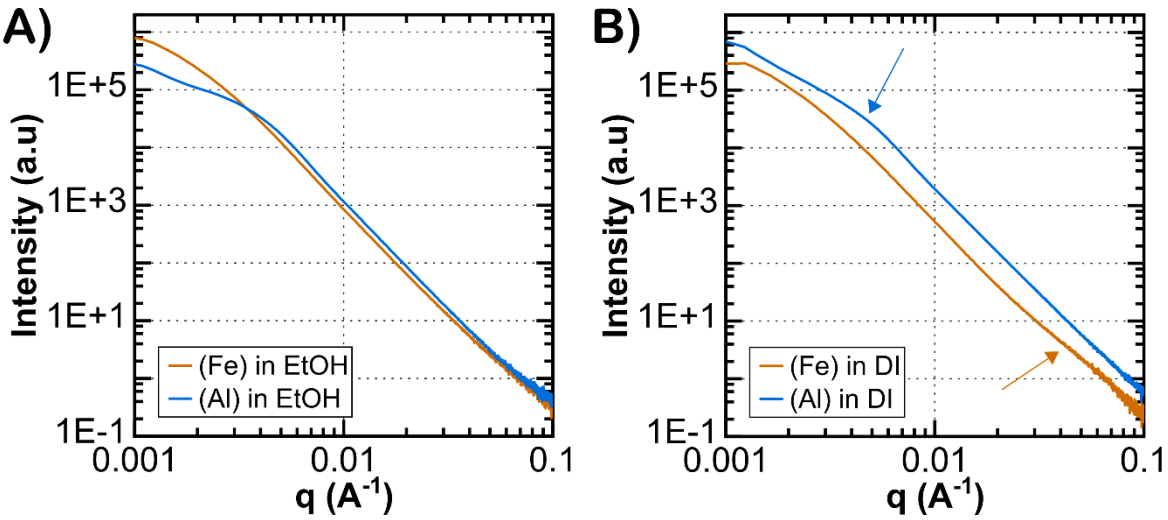

Figure 8. Typical SAXS patterns of original nanoMIL-100(Al) and (Fe) suspensions in (A) ethanol absolute (EtOH) and (B) deionized water (DI).

The differences between the two nanoMIL-100 are significantly noticeable during their degradation. Figure 9 shows how the SAXS patterns evolve when incubating nanoMIL-100(Al) and nanoMIL-100(Fe) in PBS at different input P/M ratios, i.e., very low (0.3), low (0.5), and moderate (5.5). Among the three chosen reaction ratios, the most dramatic changes upon degradation were expectedly witnessed at moderate input P/M 5.5. At this ratio, the SAXS patterns of the corresponding degraded nanoMIL-100(Fe) (Figure 9C) have a gradually growing scattering tail starting above 0.02 $Å^{-1}$, which could qualitatively indicate a surface roughening[52] or a nano-texturization such as internal hole formation. The surface roughening of nanoMIL-100(Fe) particles was already observed by Li et al., who reported TEM images of degraded particles with rounded edges.[39] For the 48h-degraded MIL-100(Fe) at moderate P/M, the deviation of the curve from its original algebraic law is above 0.02 $Å^{-1}$, which is hardly compatible with an increase in surface roughness. Still, the size of this structure alteration at the surface or inside cannot be

considered small compared to the particle size. Despite surface roughening and/or alteration inside the volume, SEM images show that the degraded MIL-100(Fe), even at a high P/M 11, are still distinguishable particles, and the global shape and size of the particles are conserved (Figure 10D-F).

A different phenomenon was observed in the degradation of nanoMIL-100(Al). A second upturn appears around 0.05 $Å^{-1}$ in SAXS patterns in Figure 9D-F (note that this q position depends on P/M). This new feature appears more rapidly during the degradation process with higher P/M ratios. A definitive pattern is obtained almost immediately for P/M of 5.5 (Figure 9F). Another striking point is the concomitant disappearance of the first upturn at 0.005 $Å^{-1}$. The SEM image of the corresponding degraded MIL-100(Al) (Figure 9A-C and S23B) displays aggregates of particles much smaller than the original ones, creating a cauliflower shape. The upturn around 0.05 $Å^{-1}$ is possibly the correlation distance between the small grains of this cauliflower structure. Furthermore, the q^{-2} slope below 0.05 $Å^{-1}$ (Figure 9F) shows that the small grains appear over the large particles, corresponding to the aggregation of objects seen by SEM (Figure 10C). These large aggregates and agglomerates cannot be seen by SAXS because their size exceeds the *q*-range accessible on the synchrotron's SWING beamline.

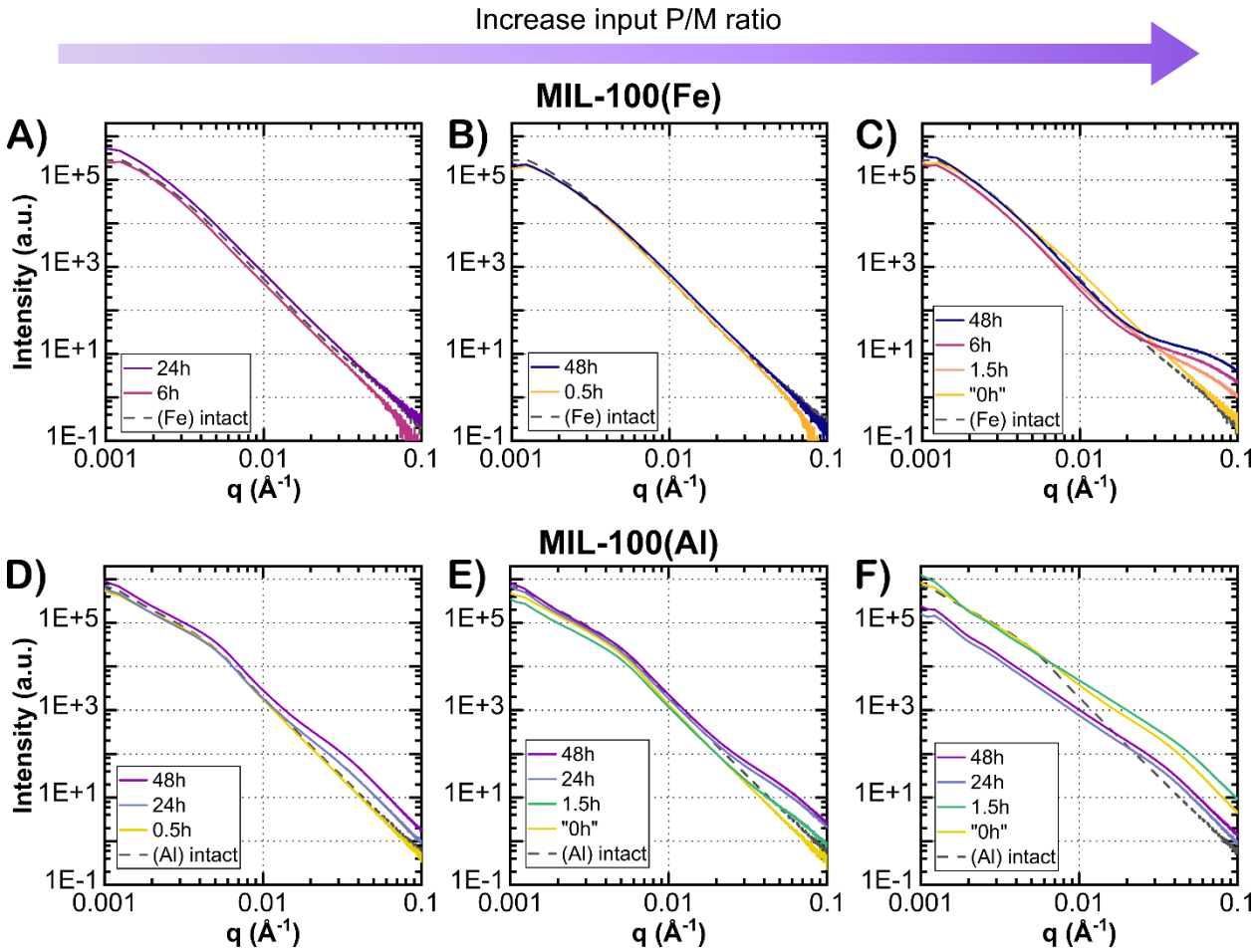

Figure 9. Time evolution of SAXS patterns of degraded (A, B, C) nanoMIL-100(Fe) and (D, E, F) nanoMIL-100(Al) suspensions under different input P/M ratios: very low (0.3), low (0.5), and moderate (5.5). For the sample "0 h" time point, PBS was mixed with nanoMOF in a few seconds, followed by centrifugation to separate the degraded MOF from PBS (details see experimental section).

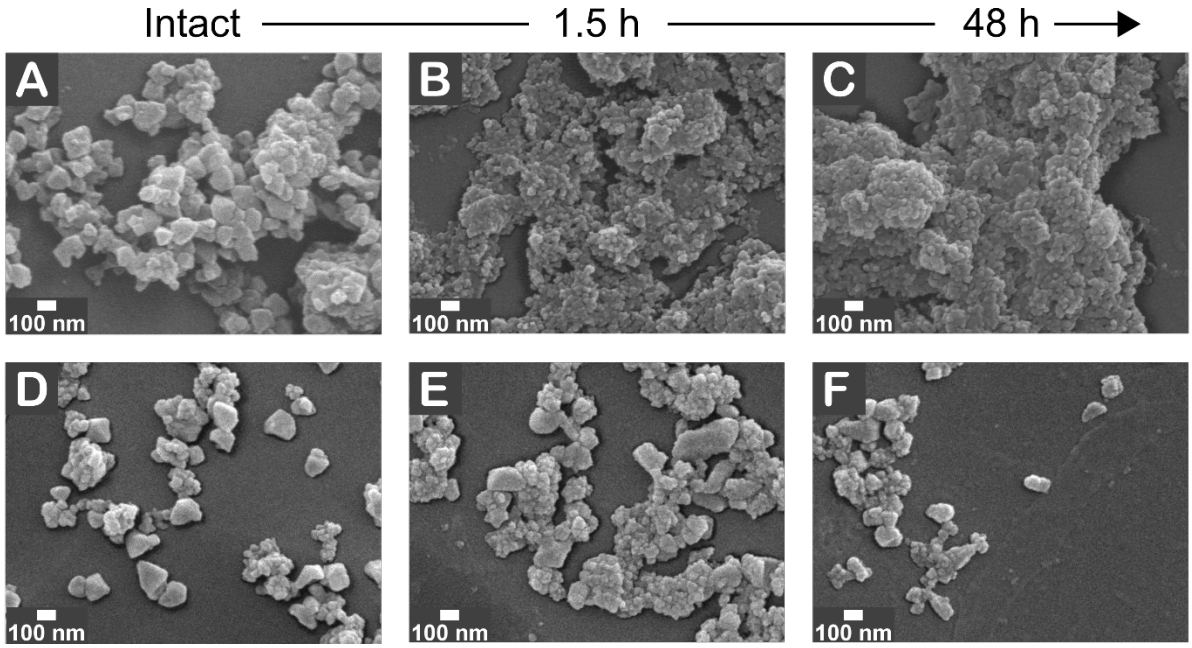

Figure 10. Time evolution of SEM images of (A-C) original and degraded nanoMIL-100(Al), and (D-F) original and degraded nanoMIL-100(Fe). NanoMOF degradation was performed with high input P/M 11 and a duration of 1.5 h (B and E) and 48 h (C and F). The final concentration of SEM's sample was 0.5 $mg.mL^{-1}$.

At very low and low input P/M ratios (0.3 and 0.5, respectively), the morphological transformation during degradation of the two MIL-100 MOFs is less pronounced. At these ratios, there is no change in the scattering curves of degraded nanoMIL-100(Fe) compared to the original one (Figure 9A-B). Consistently, SEM images for P/M 0.3 show degraded MIL-100(Fe) particles mostly have a similar shape and size to intact particles and with some aggregation (Figure S23D-F). The SAXS data of nanoMIL-100(Al) at the same conditions offer a different view of the degradation's intermediate stage. NanoMIL-100(Al) particles are still transformed into a cauliflower structure (Figure S24A, S23A-C), as in the case of moderate P/M 5.5. However, the first upturn at 0.005 $Å^{-1}$ does not progressively shift to 0.05 $Å^{-1}$ but disappears along with the appearance of the second one (Figure 9D-E). It seems that the MIL-100(Al) particle morphological

evolution is not progressive but a sudden size decrease of all particles, eventually leading to aggregation. The first steps of the degradation create a barrier to the process, but once it has started, it progresses faster.

The degradation of modified nanoMIL-100 was monitored in the same way by combining SAXS and electron microscopy. First, the chemical modifications, including CDP coating, ATP and AMP drug loading, do not affect either the size, shape, or aggregation state of the MIL-100, as testified by the SAXS patterns (Figure S25) and the TEM images (Figure S26-S27). For nanoMIL-100(Fe), the ATP/AMP drug loading and CDP surface coating do not alter the degradation process of nanoMIL-100(Fe) particles. The SAXS pattern of degraded drug-loaded, degraded surface-coated, and degraded original nanoMIL-100(Fe) are nearly reminiscent (Figure S28). The time evolution of MIL-100(Fe)'s SAXS curves remains unchanged, whatever the modification.

A different scenario (Figure 11) is witnessed for the degradation of modified nanoMIL-100(Al). The general trend observed in the degradation of original nanoMIL-100(Al) is maintained, i.e., the disappearance of the first upturn at 0.005 $Å^{-1}$ along with the appearance of the one at 0.5 $Å^{-1}$. However, the process is slowed down for the drug-loaded nanoMIL-100(Al) (Figure 11A-C). This phenomenon is more prominent for the ATP-loaded MOF than for AMP-loaded. Regarding the CDP-coated nanoMIL-100(Al), the evolution upon degradation differs (Figure 11D-F). Firstly, the first upturn at 0.005 $Å^{-1}$ remains even at the moderate P/Al, suggesting that the global shape of the nanoMIL-100(Al) particle remains. Secondly, the position of the upturn at high q depends on the P/Al; the higher the P/Al, the higher the q position, and the smaller the cauliflower structure. The reasons for this impact of CDP coating remain unclear.

Overall, the encapsulated ATP and AMP and the CDP surface coating only influence the degradation process of nanoMIL-100(Al) but not the iron analog case.

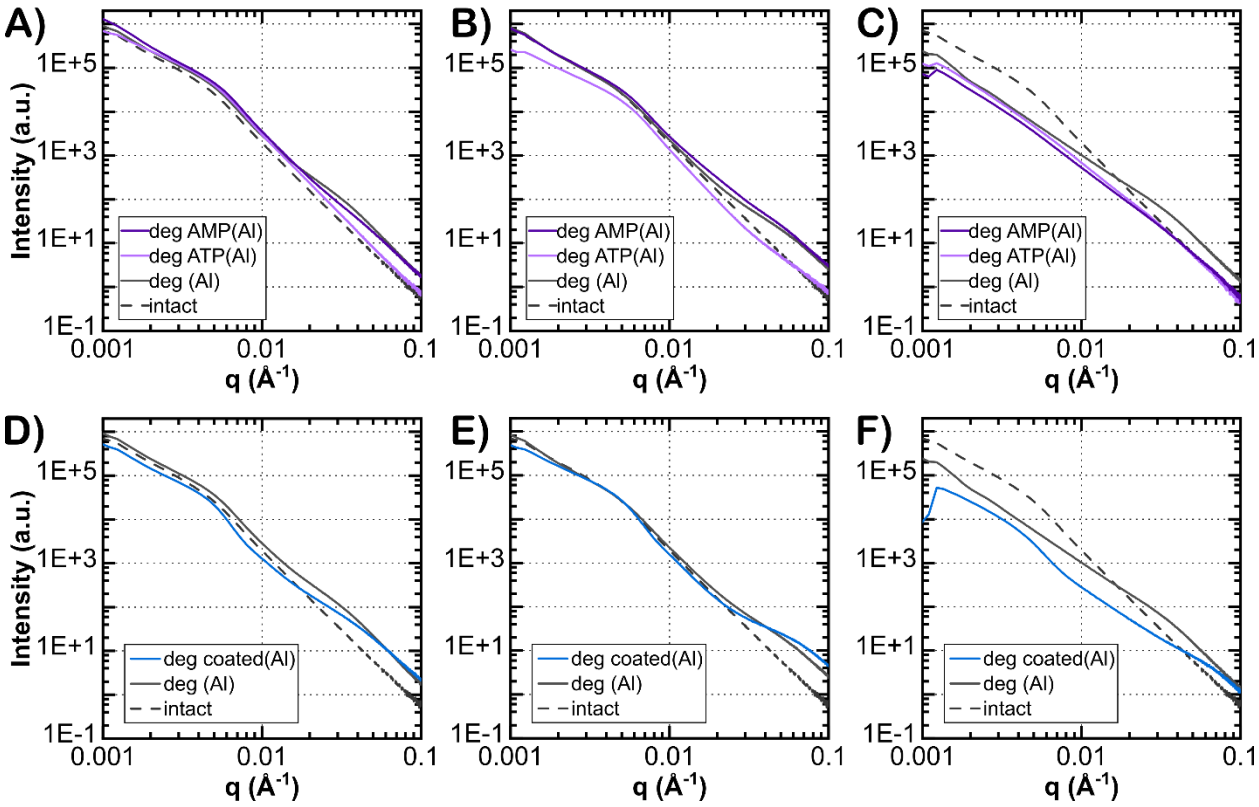

Figure 11. (A-C) SAXS patterns of 48-hour-degraded ATP- and AMP-loaded nanoMIL-100(Al) at P/Al 0.3, 0.5, and 5.5, respectively. (D-F) SAXS patterns of 48-hour-degraded CDP-coated nanoMIL-100(Al) at the same series of P/Al ratios. The patterns of degraded original and intact MOFs were plotted for comparison.

3.3.2. Interaction between nanoMIL-100 and water

Different degradation behaviors of nanoMIL-100 at the nanoscopic scale, probed by X-ray scattering and electron microscopy above, could be directly related to some specific interaction between water and MIL-100 NPs in their aqueous suspensions. As MIL-100 is micro/mesoporous, water molecules inside the micropores, on the surface, and outside the NPs can interact differently with the MIL-100 NPs, hence different roles in the NP degradation. During the nanoMOF

degradation reaction, water molecules act as a solvent for transporting reactants and products and are directly involved in the initial reaction steps. Then, the behaviors of the surface and pore water molecules strongly interacting with particles could change more than the bulk water. Therefore, probing the behavior of water could be a way to follow the degradation process of nanoMIL-100. In this study, we examined these hypotheses using NMR relaxometry. This technique, being particularly sensitive to interfacial dynamics,[53–55] is appropriate to investigate the exterior and interior surface of nanoMOF upon its degradation. Relaxometry measurements on nanoMIL-100 aqueous suspension were carried out from room to low temperature. The idea is to freeze the bulk water to selectively probe the water at the particle surface or inside the pores. The appropriate temperature for the low-field relaxometry measurements was determined as -15 °C by high-field NMR measurements (see SI for details, Figure S29-S32).

The ^{1}H NMR dispersion (NMRD) profiles of original, AMP-, and ATP-loaded MIL-100(Al) and their degraded samples are presented in Figure 12A-B. Looking at Figure 12A, the drug loading does not modify the curve's general shape, except for the plateau's value at low field and its cut-off frequency. The ^{1}H NMRD profiles nearly superimpose at the high-frequency range, i.e., above 0.5 MHz, whilst the plateau value increases in the following order: empty MIL-100(Al) > AMP-loaded > ATP-loaded samples. Along with this increase, the cut-off frequently shifts slightly to lower values in the same order: empty MIL-100(Al) > AMP-loaded > ATP-loaded samples. These phenomena indicate that the water dynamics inside nanoMIL-100(Al) and its interaction with the pore wall remain nearly the same and are only marginally hindered by the presence of the drug molecules. The plateau value can be associated with when the water escapes from its confined environment, usually from a surface.[56] In the present case, the cut-off frequency can be linked to the time water moves from the pore network to the particle surface. The escape time converted

from the cut-off frequency is 1-2 μs. If one considers a Brownian diffusion of water in the three dimensions with a self-diffusion coefficient equal to 2×10^{-9} $m^2.s^{-1}$, the explored distance is around 100 nm, equal to the average MOF's particle size. Therefore, the shift in the cut-off frequency and the increase in the plateau suggest that encapsulated drug molecules increase the apparent tortuosity for water molecules.

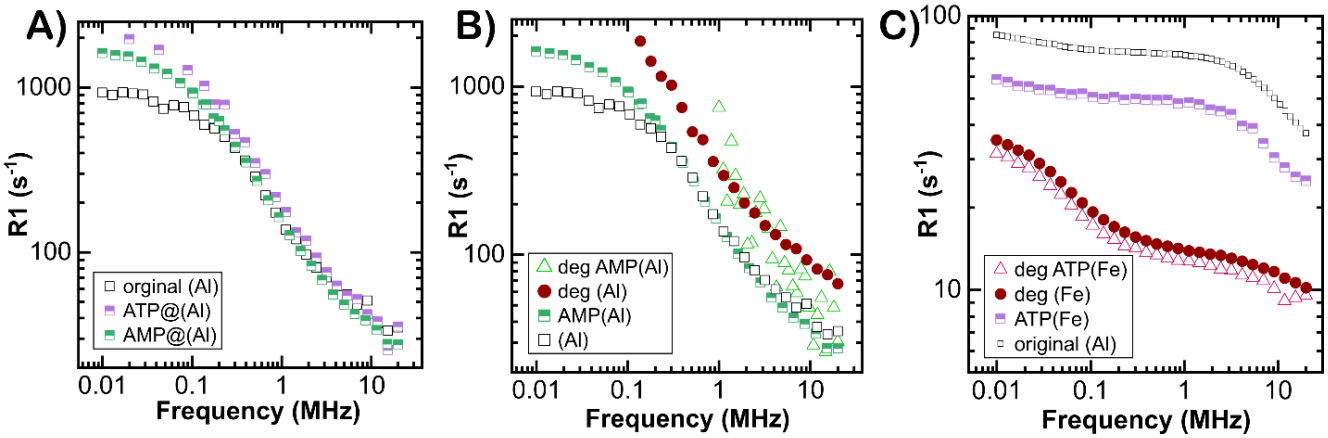

Figure 12. (A) ^{1}H NMRD profiles of ATP and AMP-drug loaded nanoMIL-100(Al), in comparison with original MOF, recorded at -15°C. (B) ^{1}H NMRD profiles of degraded AMP-loaded nanoMIL-100(Al), compared with original, AMP-loaded, and degraded AMP-loaded MOFs, recorded at -15 °C. (C) ^{1}H NMRD profile of degraded nanoMIL-100(Fe) without or with the loaded ATP compared to the samples before degradation, recorded at 25 °C. The initial MOF concentration of all samples is 25 mg.mL^{-1}.

Using the same acquisition conditions for the degraded samples, the recorded signal (NMR FID) drops as compared with the non-degraded samples, showing the loss of the MOF porosity (Figure 12B). This phenomenon is much stronger for the drug-loaded samples, hence greater uncertainty in the R_1 values. The R_1 values of degraded samples are higher than the corresponding non-degraded samples. In addition, the change in the slope of the NMRD profiles upon degradation indicates modification of the water/surface interaction during the degradation processes.

In contrast to nanoMIL-100(Al), the NMR relaxometry measurement of nanoMIL-100(Fe) was conducted at room temperature. Due to the paramagnetic Fe(III), keeping the water confined in the nanoMIL-100(Fe) by freezing the sample at -15°C leads to a complete magnetization loss before one can carry out the R_1 measurement. Consequently, the relaxometry measurement of nanoMIL-100(Fe) suspension at room temperature mainly reflects the molecular motions of bulk water at the external surface of MOF particles. Regarding the original nanoMIL-100(Fe), its NMRD profile shape (Figure 12C) shows the influence of the Fe(III) on the ^{1}H magnetization relaxation,[57] when paramagnetic centers are buried under the surfaces.[58] Upon degradation of nanoMIL-100(Fe), its NMRD profile is significantly modified. The obtained shape is typical for water interacting with a paramagnetic center.[59,60] Moreover, the ratio R_1(low field)/R_1(high field) of the degraded samples is nearly equal to 10/3, the characteristic value of the Solomon equation for a nuclear relaxation due to the electron-nucleus dipolar interaction.[61] This feature demonstrates that the water molecules can come in close contact with Fe(III) ions. In this model, R_1 decreases as r^6, where r is the distance between the ^{1}H of water and Fe(III) ion. The transformation of NMRD profiles of nanoMIL-100(Fe) after degradation indicates the exposure of Fe(III) at the nanoMOF's outer surface changes. One reason could be the formation of an iron phosphate layer at the nanoMIL-100(Fe) surface due to its degradation reaction with phosphate. Also, notice from Figure 12C that the degraded nanoMIL-100(Fe) has a lower relaxation rate than the intact NPs. Suppose the number of MOF particles does not change. In that case, this reduction in relaxation rate signifies a less intense paramagnetic effect of Fe(III). A possible explanation is a decrease in the number of iron sites accessible to bulk water or different paramagnetic properties between iron trimesate and iron phosphate.

In addition, the ATP encapsulation does not substantially impact the NMRD profiles of either non-degraded or degraded nanoMIL-100(Fe). The NMRD profiles before and after degradation of the ATP-loaded nanoMIL-100(Fe) have similar shapes to those of empty MOF (Figure 12C). The drug is supposed to be located exclusively inside MOF cages and not at its surface, thus not influencing the accessibility of water to surface iron sites.

3.4.Discussion on the Erosion Process of NanoMIL-100

The two analogs, nanoMIL-100(Al) and nanoMIL-100(Fe), are likely to react with phosphate in PBS with the same reaction steps but degrade with different rates and reactivity. Thus, they are eroded in different ways.

The two nanoMIL-100 MOFs have comparable porosity, cage size, and pore opening window. Also, phosphate is smaller than the MIL-100 pore window. Accordingly, phosphate ions can penetrate these porous nanoMOFs through the pore window and react with the metallic centers. This argument is valid when there is no barrier for phosphate diffusion, but any pore-closing event could hinder the action of phosphate ions.

NanoMIL-100(Fe) seems to preferentially undergo surface erosion, judging from its high affinity towards phosphate and progressive trimesate release profile (lqNMR). When the P/Fe molar ratio is not high enough to cause complete trimesate release, the accumulation of iron phosphate passivates the nanoMIL-100(Fe) surface and reduces its porosity (N_2 adsorption). Accordingly, the phosphate diffusion is limited, and the degradation and erosion rates decrease with time. The surface erosion mechanism also fits the linear increase in surface P/Fe ratio (XPS) and non-linear increase in bulk P/Fe ratio (EDS) as a function of % trimesate release. Nevertheless, a typical signature of classic surface erosion, the decrease in DDS's size over time, is not observed (SAXS). Note that the surface roughness of nanoMIL-100(Fe) did not modify significantly at very

low and low degradation ratios (0.3 and 0.5, respectively) but at a moderate value of 5.5. We hypothesize that degradation at low-range input P/Fe ratios produces an iron phosphate shell surrounding the intact MIL-100(Fe) core. As a result, the degraded nanoMIL-100(Fe) retains the original particle shape and size.

For nanoMIL-100(Al), surface erosion appears to occur at low input P/Al ratios (0.3 and 0.5), based on its progressive trimesate release profile (lqNMR) and the presence of small species at nanoMIL-100(Al) surface (TEM). The porosity of aluminum MOF decreases to a larger extent than in iron MOF. At an increasing input P/Al ratio that can induce total degradation of nanoMIL-100(Al), the phosphate penetration is fast enough to react with nanoMIL-100(Al) before the passivation occurs. One can imagine that nanoMIL-100(Al) quickly disintegrates and transforms into smaller aluminum phosphate particles (SEM, SAXS). That kind of bulk erosion could lead to non-controlled trimesate ligand release and concomitant continuous increase in bulk and surface P/Al ratio. Note that the initial nanoMIL-100(Al) in water exists as agglomerates, unlike nanoMIL-100(Fe), which exists as separate particles.

All in all, the nanoMOF erosion process is governed by a combination of successive processes: phosphate penetration, phosphate substitution, surface passivation, and pore closure, as illustrated schematically in Figure 13. Two types of erosion mechanisms are observed depending on the metal center in the nanoMOF. With MIL-100(Fe), surface erosion is responsible for gradual and controlled degradation and drug release. Whereas with MIL-100(Al), having an abrupt surface roughness caused by bulk erosion, degradation and drug release processes occur fast and uncontrollably.

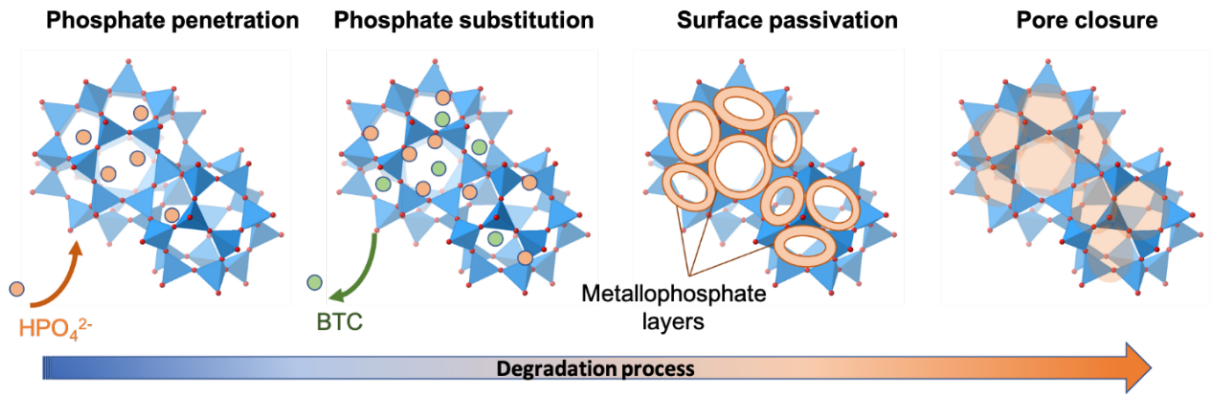

Figure 13. Schematic representation of successive steps occurring during the nano-MIL-100 degradation process in PBS.

4. CONCLUSIONS

This study presents the degradation and erosion mechanisms of two nanoMIL-100 drug carriers in phosphate buffer, a simulated physiological medium. Similar and different properties and behaviors of iron- and aluminum-based MIL-100 analogs towards degradation, drug encapsulation, and drug release were found. Moreover, a multi-technique strategy has been used to investigate the molecular and nanoscopic aspects of the degradation, providing a complete description of degradation reaction and material erosion.

At the molecular scale, we prove that nanoMIL-100(Al) and nanoMIL-100(Fe) experience similar reaction steps with phosphate. Using spectroscopy techniques, including lqNMR, XPS, IR, and EDS, the nature, quantity, and composition of the degradation products at liquid and solid phases were identified. Ligand substitution by phosphate ions is the principal driving force behind the degradation reaction. The degradation reaction could progress following two possibilities depending on the input P/M ratio. Suppose the input P/M ratio is not high enough to induce the total release of trimesate ligands. The development of metal phosphate complexes at the nanoMOF

surface partially blocks access of phosphate to the nanoMOF, thus slowing down the degradation reaction. When the input P/M ratio is sufficient to make the coordination between phosphate and the Al/Fe metal centers faster than the surface passivation, nanoMIL-100 could be transformed into metal (hydroxy)phosphate.

Furthermore, our investigation demonstrates the impact of drug encapsulation on the nanoMOF degradation, hence its drug release process. The main affecting factor is the introduction of new metal-ligand bonds and their relative strength to existing ones. The triphosphate-bearing drug ATP, which interacts more strongly with nanoMIL-100 than its monophosphate derivative AMP, could compete with the degrading agent, phosphate ions, and alter the MIL-100 carrier degradation and drug release.

At the nanoscale, nanoMIL-100(Al) and nanoMIL-100(Fe) exhibit different behaviors and interactions with the surrounding water in their suspension that can correlate to the molecular scale's degradation mechanism. X-ray scattering and electronic microscopy illustrate the size and morphological evolutions of MIL-100 NPs during degradation. On the one hand, MIL-100(Fe) NPs react as individual particles and maintain their global size and morphology. Starting from a certain P/Fe ratio that causes a high degree of degradation, the degraded nanoMIL-100(Fe) undergoes gradual surface roughening due to the formation of iron phosphate. On the other hand, the growth of small aluminum phosphate particles on MIL-100(Al) agglomerates results in a more abrupt surface roughening. These aluminum phosphate particles aggregate when the nanoMIL-100(Al) is about to be fully degraded. Finally, NMR relaxometry data show different types of interaction between water and nanoMIL-100(Al)/nanoMIL-100(Fe) in their aqueous suspension. Degradation and drug encapsulation induce reduced mobility of water inside MOF pores and altered accessibility to surface metal sites. These qualitative results could be further developed in

future work by modeling NMR relaxometry data to calculate the dynamic parameters of pore/surface and bulk water.

A possible outcome of this work is the transfer of the multi-scale approach presented here to study the degradation process of other families of MOFs and porous systems, whether diamagnetic or paramagnetic. It is also beneficial to investigate MOF degradation under more complex conditions, e.g., a combination of coordinating anions including phosphate, sulfate, and carbonate, as well as conditions closer to the actual physiological environment in the human body. Expanding current knowledge of nanoMIL-100 chemistry achieved in this study may help to rationalize better future drug delivery performance data.

ASSOCIATED CONTENT

Supporting Information. The supporting information contains: 1) details of experimental procedures for nanoMIL-100 synthesis and characterization, drug encapsulation, surface modification, degradation, and drug release, 2) characterization results of original nanoMIL-100(Al) and nanoMIL-100(Fe): DLS, TEM, SEM, PXRD, BET, IR, TGA, 3) characterization results of degraded original nanoMIL-100(Al) and nanoMIL-100(Fe): ^{31}P and ^{1}H NMR, PXRD, BET, IR, XPS, 4) drug payload wt% and encapsulation efficiency of ATP and AMP in nanoMIL-100, liquid chromatogram, ^{27}Al and ^{31}P MAS NMR of drug-loaded nanoMIL-100(Al), 5) additional results of SAXS, TEM, SEM measurement of drug-loaded and degraded drug-loaded nanoMIL-100, and 6) ^{1}H NMR of nanoMIL-100(Al) and nanoMIL-100(Fe) at low temperature. The file is available free of charge *via* the Internet at http://pubs.acs.org.

AUTHOR INFORMATION

Authors

Mai Dang Le Vuong

Yuliia Horbenko

Mathieu Frégnaux

Ioanna Christodoulou

Charlotte Martineau-Corcos

Pierre Levitz

Author Contributions

C.M.C., M.H., A.L.R., and R.G. conceived the idea and designed the experiments. M.D.L.V., Y.H., and I.C. synthesized and characterized the materials. M.F. and Y.H. performed the XPS experiments. A.L.R., P.L., and M.D.L.V. performed and analyzed SAXS and NMR relaxometry measurements. M.D.L.V. and C.M.C. collected and analyzed solid-state NMR data. All authors participated in the data discussion. M.D.L.V. and M.H. wrote the manuscript, and all authors revised the manuscript. All authors have approved the final version of the manuscript.

Notes

The authors declare no competing financial interest.

ACKNOWLEDGMENT

This work was supported by the Paris Ile-de-France Region – DIM "Respore" and a public grant overseen by the French National Research Agency as part of the "Investissements d'Avenir" program (Labex Charm3at, ANR-11-LABX-0039-grant). The authors acknowledge the SOLEIL synchrotron for awarding beam time on beamline SWING through the BAG scheme No. 20201118. The authors are grateful for the access to the NMR relaxometry platform RELAXOME of Fédération de Chimie et Matériaux de Paris-Centre funded by Région Ile de France, Sorbonne University, and CNRS. CMC thanks Dr. Marianna Porcino (CEMHTI – CNRS, France) for recording the 17.6 T NMR spectra. Financial support from the IR INFRANALYTICS FR2054 for conducting the research is gratefully acknowledged.

REFERENCES

(1) Batten, S. R.; Champness, N. R.; Chen, X.-M.; Garcia-Martinez, J.; Kitagawa, S.; Ohrstrom, L.; O'Keeffe, M.; Suh, M. P.; Reedijk, J. Terminology of Metal-Organic Frameworks and Coordination Polymers (IUPAC Recommendations 2013). *Pure Appl. Chem.* **2013**, *85*, 1715–1724.

(2) Zhao, T.; Luo, M.; Zou, M.; Nie, S.; Li, X. Advances in Nano-Sized Metal-Organic Frameworks and Biomedical Applications: A Review. *J. Biomed. Nanotech.* **2022**, *18*, 1707–1727.

(3) Wyszogrodzka, G.; Marszalek, B.; Gil, B.; Dorozynski, P. Metal-Organic Frameworks: Mechanisms of Antibacterial Action and Potential Applications. *Drug Dis. Today* **2016**, *21*, 1009–1018.

(4) Lawson, H. D.; Walton, S. P.; Chan, C. Metal–Organic Frameworks for Drug Delivery: A Design Perspective. *ACS Appl. Mater. Interfaces* **2021**, *13*, 7004–7020.

(5) Della Rocca, J.; Liu, D.; Lin, W. Nanoscale Metal–Organic Frameworks for Biomedical Imaging and Drug Delivery. *Acc. Chem. Res.* **2011**, *44*, 957–968.

(6) Simon-Yarza, T.; Mielcarek, A.; Couvreur, P.; Serre, C. Nanoparticles of Metal-Organic Frameworks: On the Road to In Vivo Efficacy in Biomedicine. *Adv. Mater.* **2018**, *30*, 1707365.

(7) Horcajada, P.; Gref, R.; Baati, T.; Allan, P. K.; Maurin, G.; Couvreur, P.; Ferey, G.; Morris,

R. E.; Serre, C. Metal-Organic Frameworks in Biomedicine. *Chem. Rev.* **2012**, *112*, 1232–1268.

(8) Wang, L.; Li, Z.; Wang, Y.; Gao, M.; He, T.; Zhan, Y.; Li, Z. Surface Ligand-Assisted Synthesis and Biomedical Applications of Metal-Organic Framework Nanocomposites. *Nanoscale* **2023**, *15*, 10529–10557.

(9) Tohidi, S.; Aghaie-Khafri, M. Cyclophosphamide Loading and Controlled Release in MIL-100(Fe) as an Anti-Breast Cancer Carrier: In Vivo In Vitro Study. *Curr. Drug Deliv.* **2023**, 21, 283-294.

(10) Ding, M.; Liu, W.; Gref, R. Nanoscale MOFs: From Synthesis to Drug Delivery and Theranostics Applications. *Adv. Drug Deliv. Rev.* **2022**, *190*, 114496.

(11) Steenhaut, T.; Filinchuk, Y.; Hermans, S. Aluminium-Based MIL-100(Al) and MIL-101(Al) Metal-Organic Frameworks, Derivative Materials and Composites: Synthesis, Structure, Properties and Applications. *J. Mater. Chem. A* **2021**, *9*, 21483–21509.

(12) Singh, N.; Qutub, S.; Khashab, N. M. Biocompatibility and Biodegradability of Metal Organic Frameworks for Biomedical Applications. *J. Mater. Chem. B* **2021**, *9*, 5925–5934.

(13) Ettlinger, R.; Laechelt, U.; Gref, R.; Horcajada, P.; Lammers, T.; Serre, C.; Couvreur, P.; Morris, R. E.; Wuttke, S. Toxicity of Metal-Organic Framework Nanoparticles: From Essential Analyses to Potential Applications. *Chem. Soc. Rev.* **2022**, *51*, 464–484.

(14) Velasquez-Hernandez, M. de J.; Ricco, R.; Carraro, F.; Limpoco, F. T.; Linares-Moreau, M.; Leitner, E.; Wiltsche, H.; Rattenberger, J.; Schroettner, H.; Fruehwirt, P.; Stadler, E. M.; Gescheidt, G.; Amenitsch, H.; Doonan, C. J.; Falcaro, P. Degradation of ZIF-8 in Phosphate Buffered Saline Media. *Crystengcomm* **2019**, *21*, 4538–4544.

(15) Buzek, D.; Adamec, S.; Lang, K.; Demel, J. Metal-Organic Frameworks vs. Buffers: Case Study of UiO-66 Stability. *Inorg. Chem. Front.* **2021**, *8*, 720–734.

(16) Horcajada, P.; Serre, C.; Maurin, G.; Ramsahye, N. A.; Balas, F.; Vallet-Regi, M.; Sebban, M.; Taulelle, F.; Ferey, G. Flexible Porous Metal-Organic Frameworks for a Controlled Drug Delivery. *J. Am. Chem. Soc.* **2008**, *130*, 6774–6780.

(17) Quijia, C. R.; Lima, C.; Silva, C.; Alves, R. C.; Frem, R.; Chorilli, M. Application of MIL-100(Fe) in Drug Delivery and Biomedicine. *J. Drug Deliv. Sci. A* **2021**, *61*, 102217.

(18) Qi, X.; Shen, N.; Al Othman, A.; Mezentsev, A.; Permyakova, A.; Yu, Z.; Lepoitevin, M.; Serre, C.; Durymanov, M. Metal-Organic Framework-Based Nanomedicines for the Treatment of Intracellular Bacterial Infections. *Pharmaceutics* **2023**, *15*, 1521.

(19) Horcajada, P.; Serre, C.; Vallet-Regi, M.; Sebban, M.; Taulelle, F.; Ferey, G. Metal-Organic Frameworks as Efficient Materials for Drug Delivery. *Angew. Chem.-Int. Edit.* **2006**, *45*, 5974–5978.

(20) Mehata, A. K.; Vikas, V.; Viswanadh, M. K.; Muthu, M. S. Theranostics of Metal-Organic Frameworks: Image-Guided Nanomedicine for Clinical Translation. *Nanomedicine* **2023**, *18*, 695–703.

(21) Livesey, T. C.; Mahmoud, L. A. M.; Katsikogianni, M. G.; Nayak, S. Metal-Organic Frameworks and Their Biodegradable Composites for Controlled Delivery of Antimicrobial Drugs. *Pharmaceutics* **2023**, *15*, 274.

(22) Horcajada, P.; Surble, S.; Serre, C.; Hong, D.-Y.; Seo, Y.-K.; Chang, J.-S.; Greneche, J.-M.; Margiolaki, I.; Ferey, G. Synthesis and Catalytic Properties of MIL-100(Fe), an Iron(III) Carboxylate with Large Pores. *Chem. Commun.* **2007**, 2820–2822.

(23) Zhong, G.; Liu, D.; Zhang, J. Applications of Porous Metal-Organic Framework MIL-100(M) (M = Cr, Fe, Sc, Al, V). *Cryst. Growth Des.* **2018**, *18*, 7730–7744.

(24) Li, J.; Peng, H.; Ji, W.; Lu, D.; Wang, N.; Peng, C.; Zhang, W.; Li, M.; Li, Y. Advances in Surface-Modified Nanometal-Organic Frameworks for Drug Delivery. *Int. J. Pharm.* **2023**, *642*, 123119.

(25) Rodriguez-Ruiz, V.; Maksimenko, A.; Anand, R.; Monti, S.; Agostoni, V.; Couvreur, P.; Lampropoulou, M.; Yannakopoulou, K.; Gref, R. Efficient "Green" Encapsulation of a Highly Hydrophilic Anti-cancer Drug in Metal-Organic Framework Nanoparticles. *J. Drug Targ.* **2015**, *23*, 759–767.

(26) Horcajada, P.; Chalati, T.; Serre, C.; Gillet, B.; Sebrie, C.; Baati, T.; Eubank, J. F.; Heurtaux, D.; Clayette, P.; Kreuz, C.; Chang, J.-S.; Hwang, Y. K.; Marsaud, V.; Bories, P.-N.; Cynober, L.; Gil, S.; Ferey, G.; Couvreur, P.; Gref, R. Porous Metal-Organic-Framework Nanoscale Carriers as a Potential Platform for Drug Delivery and Imaging. *Nat. Mater.* **2010**, *9*, 172–178.

(27) Agostoni, V.; Chalati, T.; Horcajada, P.; Willaime, H.; Anand, R.; Semiramoth, N.; Baati, T.; Hall, S.; Maurin, G.; Chacun, H.; Bouchemal, K.; Martineau, C.; Taulelle, F.; Couvreur, P.; Rogez-Kreuz, C.; Clayette, P.; Monti, S.; Serre, C.; Gref, R. Towards an Improved Anti-HIV Activity of NRTI via Metal-Organic Frameworks Nanoparticles. *Adv. Healthcare Mater.* **2013**, *2*, 1630–1637.

(28) Unamuno, X.; Imbuluzqueta, E.; Salles, F.; Horcajada, P.; Blanco-Prieto, M. J. Biocompatible Porous Metal-Organic Framework Nanoparticles Based on Fe or Zr for Gentamicin Vectorization. *Eur. J. Pharm. Biopharm.* **2018**, *132*, 11–18.

(29) Taherzade, S. D.; Rojas, S.; Soleimannejad, J.; Horcajada, P. Combined Cutaneous Therapy Using Biocompatible Metal-Organic Frameworks. *Nanomaterials* **2020**, *10*, 2296.

(30) Baati, T.; Njim, L.; Neffati, F.; Kerkeni, A.; Bouttemi, M.; Gref, R.; Najjar, M. F.; Zakhama, A.; Couvreur, P.; Serre, C.; Horcajada, P. In Depth Analysis of the in Vivo Toxicity of Nanoparticles of Porous Iron(III) Metal-Organic Frameworks. *Chem. Sci.* **2013**, *4*, 1597–1607.

(31) Feng, Y.; Wang, C.; Ke, F.; Zang, J.; Zhu, J. MIL-100(Al) Gels as an Excellent Platform Loaded with Doxorubicin Hydrochloride for PH-Triggered Drug Release and Anti-cancer Effect. *Nanomaterials* **2018**, *8*, 446.

(32) Li, X.; Porcino, M.; Qiu, J.; Constantin, D.; Martineau-Corcos, C.; Gref, R. Doxorubicin-Loaded Metal-Organic Frameworks Nanoparticles with Engineered Cyclodextrin Coatings:

Insights on Drug Location by Solid State NMR Spectroscopy. *Nanomaterials* **2021**, *11*, 945.

(33) Grall, R.; Hidalgo, T.; Delic, J.; Garcia-Marquez, A.; Chevillard, S.; Horcajada, P. In Vitro Biocompatibility of Mesoporous Metal (III; Fe, Al, Cr) Trimesate MOF Nanocarriers. *J. Mater. Chem. B* **2015**, *3*, 8279–8292.

(34) Kiss, T.; Zatta, P.; Corain, B. Interaction of Aluminium(III) with Phosphate-Binding Sites: Biological Aspects and Implications. *Coord. Chem. Rev.* **1996**, *149*, 329–346.

(35) Lijklema, L. Interaction of Orthophosphate with Iron(III) and Aluminum Hydroxides. *Environ. Sci. Technol.* **1980**, *14*, 537–541.

(36) Agostoni, V.; Anand, R.; Monti, S.; Hall, S.; Maurin, G.; Horcajada, P.; Serre, C.; Bouchemal, K.; Gref, R. Impact of Phosphorylation on the Encapsulation of Nucleoside Analogues within Porous Iron(III) Metal-Organic Framework MIL-100(Fe) Nanoparticles. *J. Mater. Chem. B* **2013**, *1*, 4231–4242.

(37) Porcino, M.; Christodoulou, I.; Vuong, M. D. L.; Gref, R.; Martineau-Corcos, C. New Insights on the Supramolecular Structure of Highly Porous Core-Shell Drug Nanocarriers Using Solid-State NMR Spectroscopy. *RSC Adv.* **2019**, *9*, 32472–32475.

(38) Bellido, E.; Guillevic, M.; Hidalgo, T.; Santander-Ortega, M. J.; Serre, C.; Horcajada, P. Understanding the Colloidal Stability of the Mesoporous MIL-100(Fe) Nanoparticles in Physiological Media. *Langmuir* **2014**, *30*, 5911–5920.

(39) Li, X.; Lachmanski, L.; Safi, S.; Sene, S.; Serre, C.; Greneche, J. M.; Zhang, J.; Gref, R. New Insights into the Degradation Mechanism of Metal-Organic Frameworks Drug Carriers. *Sci. Rep.* **2017**, *7*, 13142.

(40) Christodoulou, I.; Bourguignon, T.; Li, X.; Patriarche, G.; Serre, C.; Marliere, C.; Gref, R. Degradation Mechanism of Porous Metal-Organic Frameworks by In Situ Atomic Force Microscopy. *Nanomaterials* **2021**, *11*, 722.

(41) Vuong, M. D. L.; Christodoulou, I.; Porcino, M.; Dong, S.; Lassalle-Kaiser, B.; Haouas, M.; Gref, R.; Martineau-Corcos, C. Degradation Mechanism of Metal-Organic Framework Drug Nanocarriers Studied by Solid-State Nuclear Magnetic Resonance and X-Ray Absorption Near-Edge Structure Spectroscopy. *Chem. Mater.* **2022**, *34*, 8178–8189.

(42) Agostoni, V.; Horcajada, P.; Noiray, M.; Malanga, M.; Aykac, A.; Jicsinszky, L.; Vargas-Berenguel, A.; Semiramoth, N.; Daoud-Mahammed, S.; Nicolas, V.; Martineau, C.; Taulelle, F.; Vigneron, J.; Etcheberry, A.; Serre, C.; Gref, R. A "Green" Strategy to Construct Non-Covalent, Stable and Bioactive Coatings on Porous MOF Nanoparticles. *Sci. Rep.* **2015**, *5*, 7925.

(43) Marquez, A. G.; Demessence, A.; Platero-Prats, A. E.; Heurtaux, D.; Horcajada, P.; Serre, C.; Chang, J.-S.; Ferey, G.; Antonio de la Pena-O'Shea, V.; Boissiere, C.; Grosso, D.; Sanchez, C. Green Microwave Synthesis of MIL-100(Al, Cr, Fe) Nanoparticles for Thin-Film Elaboration. *Eur. J. Inorg. Chem.* **2012**, 5165–5174.

(44) Pearson, R.; Edgington, D.; Basolo, F. Nucleophilic Substitution Reactions in Octahedral Complexes. *J. Am. Chem. Soc.* **1962**, *84*, 3233–3237.

(45) Arp, P.; Meyer, W. Formation Constants for Selected Organometal (Al3+, Fe3+) Phosphate Complexes. *Can. J. Chem.* **1985**, *63*, 3357–3366.

(46) Hsu, P. H. Comparison of Iron(III) and Aluminum in Precipitation of Phosphate from Solution. *Water Res.* **1976**, *10*, 903–907.

(47) Kiss, T.; Sovago, I.; Martin, R. B. Aluminum(3+) Binding by Adenosine 5'-Phosphates: AMP, ADP, and ATP. *Inorg. Chem.* **1991**, *30*, 2130–2132.

(48) Sigel, H.; Becker, K.; McCormick, D. B. Ternary Complexes in Solution. Influence of 2,2′-Bipyridyl on the Stability of 1:1 Complexes of Co2+, Ni2+, Cu2+, and Zn2+ with Hydrogen Phosphate, Adenosine 5′-Monophosphate, and Adenosine 5′-Triphosphate. *Biochim. Biophys. Acta, Gen. Subj.* **1967**, *148*, 655–664.

(49) Karlik, S. J.; Elgavish, G. A.; Eichhorn, G. L. Multinuclear NMR Studies on Aluminum(III) Complexes of ATP and Related Compounds. *J. Am. Chem. Soc.* **1983**, *105*, 602–609.

(50) Khan, M. M. T.; Martell, A. E. Metal Chelates of Adenosine Triphosphate. *J. Phys. Chem.* **1962**, *66*, 10–15.

(51) Van Garderen, H.; Pantos, E.; Dokter, W.; Beelen, T.; Van Santen, R. Cluster-Cluster Aggregation and Calculated SAXS Patterns - Application to Concentration-Dependence of Fractal Parameters. *Mod. Simul. Mater. Sci. Eng.* **1994**, *2*, 295–312.

(52) Stribeck, N. Utilising Spatial Frequency Filtering to Extract Nanoscale Layer Structure Information from Isotropic Small-Angle X-Ray Scattering Data. *Colloid Polymer Sci.* **2002**, *280*, 254–259.

(53) Kimmich, R. In *Field-Cycling NMR Relaxometry. NMR: Tomography, Diffusometry, Relaxometry*; Springer, 1997; pp 138–148.

(54) Kimmich, R.; Anoardo, E. Field-Cycling NMR Relaxometry. *Prog. Nucl. Magn. Reson. Spectrosc.* **2004**, *44*, 257–320.

(55) Korb, J.-P. Multiscale Nuclear Magnetic Relaxation Dispersion of Complex Liquids in Bulk and Confinement. *Prog. Nucl. Magn. Reson. Spectrosc.* **2018**, *104*, 12–55.

(56) Levitz, P. Probing Interfacial Dynamics of Water in Confined Nanoporous Systems by NMRD. *Mol. Phys.* **2019**, *117*, 952–959.

(57) Fanost, A.; Jaber, M.; de Viguerie, L.; Korb, J.-P.; Levitz, P. E.; Michot, L. J.; Meriguet, G.; Rollet, A.-L. Green Earth Pigments Dispersions: Water Dynamics at the Interfaces. *J. Colloid Interface Sci.* **2021**, *581*, 644–655.

(58) Barberon, F.; Korb, J. P.; Petit, D.; Morin, V.; Bermejo, E. Probing the Surface Area of a Cement-Based Material by Nuclear Magnetic Relaxation Dispersion. *Phys. Rev. Lett.* **2003**, *90*, 116103.

(59) Bertini, I.; Luchinat, C.; Parigi, G.; Ravera, E. Chapter 7 - Transition Metal Ions: Shift and

Relaxation. In *NMR of Paramagnetic Molecules (Second Edition)*; Bertini, I., Luchinat, C., Parigi, G., Ravera, E., Eds.; Elsevier: Boston, 2017; pp 175–253.

(60) Fries, P. H.; Belorizky, E. Relaxation Theory of the Electronic Spin of a Complexed Paramagnetic Metal Ion in Solution beyond the Redfield Limit. *J. Chem. Phys.* **2007**, *126*, 204503.

(61) Solomon, I. Relaxation Processes in a System of 2 Spins. *Phys. Rev.* **1955**, *99*, 559–565.

TABLE OF CONTENTS GRAPHIC

For table of contents only